A new robust quadrilateral four-node variable kinematics plate element for composite structures

T.H.C. H C Le, M. d'Ottavio, P. Vidal, O. Polit

A new robust quadrilateral four-node variable kinematics plate element for composite structures

T.H.C. Le, M. D'Ottavio, P. Vidal, O. Polit

1. Introduction

The increasing use of composite laminates and sandwich structures in engineering applications drives the need for appropriate analysis and design tools with dedicated computational models. Based on geometric considerations, composite panels are conveniently modeled as two-dimensional plate/shell structures. However, complicating effects - such as anisotropy, heterogeneity and transverse shear compliance - call for plate/shell models that go beyond the so-called *classical models*, i.e., those relying on (*i*) Kirchhoff-Love assumptions and neglecting transverse deformation (Classical Laminate Plate Theory, CLPT), (*ii*) or on Reissner-Mindlin assumptions and retaining a merely constant transverse shear deformation through the thickness (First-order Shear Deformation Theory, FSDT). Numerous review papers devoted to high-order plate/shell models witness the scientific progress in this specific topic [1–5].

A useful classification discerns Equivalent Single Layer (ESL) and Layer-Wise (LW) models [6]: In the former model class, the number of unknowns is independent of the number of layers constituting the composite plate, while in the latter one, the number of unknowns increases with the number of constituting layers. CLPT and FSDT evidently pertain to the ESL models. ESL models that enhance the kinematics for the transverse shear deformation while still discarding the transverse normal deformation, are referred to as High-order Shear Deformation Theories (HSDT). Contrary to FSDT, no numerical shear correction factors are required in HSDT thanks to an at least parabolic transverse shear distribution that may also exactly verify the stress boundary conditions at the laminate's top and bottom surfaces. Seminal examples are the third-order theory by Reddy [7] and the sinus-model by Touratier [8]. Conventional ESL models employ a single approximation for the displacement field through the entire laminate's thickness; the resulting transverse strain field is continuous across the stacked layers, which contradicts the equilibrium conditions between adjacent plies with different material properties [9]. Zig-Zag models are special ESL models with a piece-wise continuous displacement field that allows to fulfill the interlaminar continuity conditions of the transverse shear stresses, see, e.g., [10,11]. The review paper by Carrera [12] offers a comprehensive discussion about the various approaches to Zig-Zag models. In presence of highly compliant core layers, or for accurately resolving local stress gradients whose wavelength is comparable to the plate thickness, it is necessary to further refine the model upon including the transverse normal deformation, see, e.g., the early contribution by Lo et al [13] and the more recent papers [14,15]. Retaining the full three-dimensional constitutive law is particularly useful for coupled problems, such as those related to thermo-mechanics [16].

In order to reduce the computational effort, it has been proposed to limit the use of expensive high-order models to those local regions

hosting the stress gradients of interest, while employing classical low-order models for the remaining large portions of the structure. Several approaches have been followed for coupling heterogeneous kinematics and their respective Finite Element (FE) approximations, see, e.g., the transition element proposed by Feng and Hoa [17] within their hybrid-mixed composite plate element formulations, the overlapping mesh approach based on Arlequin method [18], or the direct interface coupling proposed by Wenzel et al [19] on the basis of an extended variational formulation.

A very flexible manner for implementing such substructuring methods is to resort to so-called variable kinematics models and corresponding finite elements, as first pioneered by Reddy [20] and more recently systematically developed by Carrera and co-workers thanks to a dedicated Unified Formulation [21,22]. By virtue of an extensive index notation, Carrera's Unified Formulation (CUF) allows to implement a large number of finite plate/shell elements within a unique software, whose inputs provided at runtime define the actual plate/shell model to be used in the analysis [23]. Within CUF, classical displacement-based plate elements are defined through the choice of (*i*) the description at laminate level (ESL or LW), (*ii*) whether a Zig-Zag function is to be used or not, and (*iii*) the order N of the polynomial expansion assumed for the displacement field. The original version of CUF as presented by [24] has been implemented as Abaqus User Element with a dedicated Python-based preprocessing tool [25]; this package has been successfully employed in, e.g., [26,27] and forms the basis of the developments proposed in this paper.

From the computational point of view, the development of robust Finite Elements (FE) is required to cope with the adopted two-dimensional plate/shell model, see, e.g., the discussion by MacNeal [28] about the FE technology employed for Kirchhoff-Love and Reissner-Mindlin shell models. A general, highly predictive plate FE should not rely on numerical tuning coefficients, should have only six rigid body modes, for spurious zero-energy modes could be particularly detrimental, e.g., in non-linear analyses, and should be free from numerical pathologies that could degrade the solution's accuracy in case of distorted elements or extreme thickness ratios. The most characteristic example for this latter issue is transverse shear locking, a spurious over-constraint that dramatically underestimates the bending deformation of a thin, shear-deformable plate element. Several techniques have been devised for correcting the transverse shear locking pathology affecting FSDT-based plate/shell elements, most of which can be stated from hybrid-mixed approaches [29]. The most widespread techniques are reduced integration methods, which, however, require a dedicated stabilization for preventing spurious zero-energy modes [30], or so-called B-bar methods [31], in which a specific constraint is used for the transverse shear strain field. Different approaches have been followed for constructing this modified strain field, such as Kirchhoff mode [32], Assumed Natural Strain (ANS) [33,34], Mixed Interpolation of Tensorial Components (MITC) [35], the field-consistency paradigm [36], Discrete Shear elements [37] or Discrete Shear Gap (DSG) [38].

Variable kinematics plate model suffer transverse shear locking also, and the first employed countermeasures consisted in a selectively reduced quadrature [39,24,40]. Rectangular four- and nine-nodes plate elements have been been subsequently implemented upon extending the MITC approach to CUF-based high-order kinematics [41]. A four-node quadrilateral plate element has been proposed by Kulikov and Plotnikova [42] by resorting to a hybrid-mixed ANS approach in conjunction with a variable kinematics approach formulated in terms of Sampling Surfaces (SaS). In these works, *all* transverse shear strain terms issued from the high-order kinematics are constrained according to the adopted MITC or ANS approach. However, since high-order shear deformation terms depend on the plate thickness and will vanish in thin-plate limit, the locking behavior is produced by the first-order Reissner-Mindlin kinematics only. As a matter of fact, the convergence rates of CUF elements do not depend on the polynomial order N defining the plate kinematics [40].

Refined two-dimensional structural models including thickness change require special care for preventing thickness or Poisson locking, i.e., an overly stiff bending response that is produced if the transverse normal strain is not allowed to vary along the thickness direction [43]. Two class of remedies have been proposed for correctly resolving the Poisson coupling along the thickness: to retain an at least linearly varying transverse normal strain, either within an Enhanced Assumed Strain approach pioneered by Büchter et al [44], see also [45], or directly in the model kinematics [16]; or to modify the constitutive law for the bending contribution by referring to a generalized plane stress condition, as proposed, e.g., in [46].

Based on the outlined background, the present paper proposes a four-node quadrilateral element for variable kinematics displacement-based CUF plate models. A special transverse shear locking correction is formulated by referring to the field consistency paradigm and applied only to the constant, thickness-independent part of the transverse shear strain. For this, the method first proposed by Polit et al [47] for FSDT, and subsequently extended to a refined kinematics [16], is here further extended to high-order plate models with arbitrary kinematics. The resulting plate FE is implemented as User Element in the commercial package Abaqus, along with dedicated Python plug-ins for generating the model within the graphical interface of Abaqus. Following the recommendations expressed by MacNeal and Harder [48], extensive numerical tests are reported for demonstrating the absence of spurious mechanisms and assessing the element's accuracy for extreme thickness ratios as well as distorted meshes. The paper is organized as follows: the CUF-based variable kinematics approach is recalled in Section 2 and the new QC4 FE approximation is presented in Section 3. The numerical results are discussed in Section 4, where a comprehensive investigation is proposed that concerns the rank of the stiffness matrix, the robustness of the element with respect to length-to-thickness ratio and mesh distortion, as well as the accuracy of the predicted displacements and stresses for homogeneous and composite plates. Finally, Section 5 summarizes the main conclusions and proposes an outlook towards further studies.

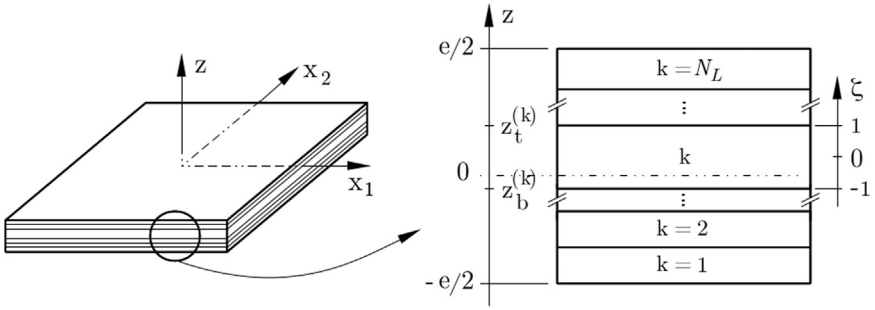

Fig. 1. Coordinates and notation used for the description of the composite plate.

2. Variable kinematics plate model

Let us consider a multilayered plate occupying the domain $V = \Omega \times \{-\frac{e}{2} \leq x_3 \leq \frac{e}{2}\}$ in a Cartesian coordinate system $(x, y, z) = (x_i)$, see Fig. 1. Unless otherwise stated, Latin indices range in {1, 2, 3}, Greek indices range in {1, 2} and tensorial repeated index convention is employed. Ω is the reference surface of arbitrary shape lying in the (x_1, x_2) − plane located for convenience at z=0. The plate has constant thickness e, which is composed of $k = 1, 2, \ldots N_L$ orthotropic, elastic and perfectly bonded layers, each with a thickness $e^{(k)}$ and with an orientation of the material orthotropy axes defined by the rotation angle $\theta^{(k)}$ about the thickness direction $x_3 \equiv z$.

2.1. The weak form of the boundary value problem

The Principle of Virtual Displacement (PVD) is employed to obtain the weak form for a displacement-based plate approximation. The volume boundary is split as $\partial V = \Gamma_u \bigcup \Gamma_\sigma$, where Γ_u is the portion with an imposed displacement field and Γ_σ is the portion with imposed tractions; without loss of generality we shall neglect body forces and pose $\Gamma_u = \partial\Omega \times \{-\frac{e}{2} \leq x_3 \leq \frac{e}{2}\}$ and $\Gamma_\sigma = \Omega \times \{-\frac{e}{2}, \frac{e}{2}\}$. The weak formulation of the problem thus reads:

For all admissible virtual displacement $\delta u_i \in \delta\mathbb{U}$, find the displacement field $u_i \in \mathbb{U}$ (space of admissible displacements) such that:

$$-\int_V \epsilon_{ij}(\delta u_l)\, \sigma_{ij}(u_m)\, \mathrm{d}x_i + \int_{\Gamma_\sigma} \delta u_i\, \bar{t}_i\, \mathrm{d}x_\alpha = 0 \tag{1}$$

where $\bar{t}_i$ are the surface loads at Γ_σ, a bar denoting prescribed values; $\epsilon_{ij}(\delta u_l)$ is the compatible virtual strain tensor and $\sigma_{ij}(u_m)$ the stress tensor defined by means of the linear elastic constitutive law in terms of the actual strains $\epsilon_{rs}(u_m)$.

2.2. Variable kinematics assumptions

Carrera's Unified Formulation (CUF) is a technique that permits to implement a large number of bi-dimensional models in a unified manner by means of an extensive use of a compact index notation [24,23]. Within the displacement-based approach, all plate theories are defined in CUF by specifying (*i*) whether the displacement field is described in Equivalent Single Layer (ESL) or Layer-Wise (LW) manner, and (*ii*) the order N of the polynomial expansion used for approximating the behavior along the thickness direction. The two-dimensional variable kinematics plate model is generally formulated upon separating the in-plane variables x_α from the thickness direction z, along which the displacement field is *a priori* postulated by known functions $F(z)$:

$$u_i(x_\alpha, z) = F_\tau(z)\, \hat{u}_{i_\tau}(x_\alpha), \tag{2}$$

where $\tau = 0, 1, \ldots, N$ is the summation index and the order of expansion N is a free parameter of the formulation. In this work N can range from 1 to 4, in agreement with the classical CUF implementation [24].

In order to deal with both ESL and LW descriptions within a unique notation, it is convenient to refer to a layer-specific thickness coordinate $z_k \in \{z_b^{(k)}, z_t^{(k)}\}$ that ranges between the z-coordinates of the bottom (subscript b) and top (subscript t) planes delimiting the k^{th} layer, see Fig. 1. Eq. (2) can thus be formally re-written for each layer as

$$u_i^{(k)}(x_\alpha, z_k) = F_t(z_k)\hat{u}_{i_t}^{(k)}(x_\alpha) + F_b(z_k)\hat{u}_{i_b}^{(k)}(x_\alpha) + F_r(z_k)\hat{u}_{i_r}^{(k)}(x_\alpha) \tag{3}$$

with $\tau = t, b, r$ and $r = 2, \ldots N$. The displacement field u_i for the whole multilayered stack is then defined through an opportune assembly procedure of the layer-specific contributions $u_i^{(k)}$, which depends on the ESL or LW description.

In an ESL approach, the thickness functions are defined as Taylor-type expansion and only one variable $\hat{u}_{i_\tau}$ is used for the whole multilayer, i.e., the layer index (k) in Eq. (3) may be dropped off and the following thickness functions are used:

$$F_b = 1, \quad F_t = z^N, \quad F_r = z^r \quad (r = 2, \ldots N-1) \tag{4}$$

The ESL description can be enhanced by including the Zig-Zag function $F_{ZZ}(z)$ proposed by Murakami in order to allow slope discontinuities at layers' interfaces [49]. In this case, the Zig-Zag function replaces the highest expansion order and the following functions are used:

$$F_b = 1, \quad F_t = F_{ZZ}(z), \quad F_r = z^r \quad (r = 2, \ldots N-1) \tag{5}$$

where Murakami's ZigZag Function (MZZF) is defined as

$$F_{ZZ}(z) = (-1)^k\, \zeta_k(z) \quad \text{with} \quad \zeta_k(z) = \frac{2}{z_t^{(k)} - z_b^{(k)}}\left(z - \frac{z_t^{(k)} + z_b^{(k)}}{2}\right) \tag{6}$$

Note that $F_{ZZ}(z)$ is expressed in terms of the non-dimensional layer-specific coordinate $-1 \leq \zeta_k \leq +1$ and it provides a linear piecewise function of bi-unit amplitude across the thickness of each layer k. More details about the use of MZZF in variable kinematics PVD-based models can be found in the paper by Demasi [50].

The assumptions for a LW description are formulated in each layer k as in Eq. (3), where the thickness functions are defined by linear combinations of Legendre polynomials $P_r(\zeta_k)$ as follows:

$$F_t(\zeta_k) = \frac{P_0(\zeta_k) + P_1(\zeta_k)}{2}; \quad F_b(\zeta_k) = \frac{P_0(\zeta_k) - P_1(\zeta_k)}{2}; \tag{7}$$
$$F_r(\zeta_k) = P_r(\zeta_k) - P_{r-2}(\zeta_k) \quad (r = 2, \ldots N)$$

where ζ_k is the non-dimensional coordinate introduced in Eq. (6). The Legendre polynomials of degree 0 and 1 are $P_0(\zeta_k) = 1$ and $P_1(\zeta_k) = \zeta_k$, respectively; higher-order polynomials are defined according to the following recursive formula:

$$P_{n+1}(\zeta_k) = \frac{(2n+1)\zeta_k\, P_n(\zeta_k) - nP_{n-1}(\zeta_k)}{n+1} \tag{8}$$

which leads to the following expressions for the polynomials employed if N=4:

$$P_2(\zeta_k) = \frac{3\zeta_k^2 - 1}{2}; \quad P_3(\zeta_k) = \frac{5\zeta_k^3 - 3\zeta_k}{2}; \quad P_4(\zeta_k) = \frac{35\zeta_k^4}{8} - \frac{15\zeta_k^2}{4} + \frac{3}{8} \tag{9}$$

It is finally emphasized that the chosen thickness functions for a LW model satisfy the following properties

$$\zeta_k = 1: \quad F_t = 1, \quad F_b = 0, \quad F_r = 0 \tag{10a}$$

$$\zeta_k = -1: \quad F_t = 0, \quad F_b = 1, \quad F_r = 0 \tag{10b}$$

Therefore, $\hat{u}_{i_t}^{(k)}$ and $\hat{u}_{i_b}^{(k)}$ are the physical displacement components at the top and bottom of the k^{th} layer, respectively, and $F_t(\zeta_k)$ and $F_b(\zeta_k)$ are the corresponding linear Lagrange interpolation functions.

2.3. The stress and strain fields

The contributions to the strain and stress fields in each layer k are identified with respect to the bending (b), transverse normal (n) and transverse shear (s) deformation of the plate:

$$\boldsymbol{\epsilon}_b^{(k)} = [\epsilon_1^{(k)}\, \epsilon_2^{(k)}\, \epsilon_6^{(k)}]; \quad \boldsymbol{\epsilon}_n^{(k)} = \epsilon_3^{(k)}; \quad \boldsymbol{\epsilon}_s^{(k)} = [\epsilon_5^{(k)}\, \epsilon_4^{(k)}]$$
$$\boldsymbol{\sigma}_b^{(k)} = [\sigma_1^{(k)}\, \sigma_2^{(k)}\, \sigma_6^{(k)}]; \quad \boldsymbol{\sigma}_n^{(k)} = \sigma_3^{(k)}; \quad \boldsymbol{\sigma}_s^{(k)} = [\sigma_5^{(k)}\, \sigma_4^{(k)}] \tag{11}$$

where Voigt's contracted notation for the symmetric strain and stress tensors has been invoked. The generic layer k is assumed to have a monoclinic material symmetry in the plate's reference frame (x_α, z); thus the linear elastic constitutive law reads in matrix form as follows

$$\begin{bmatrix} \boldsymbol{\sigma}_b^{(k)} \\ \boldsymbol{\sigma}_n^{(k)} \\ \boldsymbol{\sigma}_s^{(k)} \end{bmatrix} = \begin{bmatrix} \widetilde{\boldsymbol{C}}_{bb}^{(k)} & \widetilde{\boldsymbol{C}}_{bn}^{(k)} & \boldsymbol{0} \\ \widetilde{\boldsymbol{C}}_{bn}^{(k)T} & \widetilde{\boldsymbol{C}}_{nn}^{(k)} & \boldsymbol{0} \\ \boldsymbol{0} & \boldsymbol{0} & \widetilde{\boldsymbol{C}}_{ss}^{(k)} \end{bmatrix} \begin{bmatrix} \boldsymbol{\epsilon}_b^{(k)} \\ \boldsymbol{\epsilon}_n^{(k)} \\ \boldsymbol{\epsilon}_s^{(k)} \end{bmatrix} \tag{12}$$

where superscript T is the transposition operator. The constitutive law is obviously defined for each layer k for it depends on the layer's orthotropic elastic properties $C_{PQ}^{(k)}$ $(P, Q \in \{1, 6\})$ and on the orientation angle $\theta^{(k)}$.

Within the small strain and small displacement approximation, the linearized strain components are defined as

$$\begin{aligned} &\epsilon_i = u_{i,i} \quad \text{for} \quad i = 1, 2, 3; \\ &\epsilon_{(9-i-j)} \quad = \quad u_{i,j} + u_{j,i} \quad \text{for} \quad i, j = 1, 2, 3 \quad \text{and} \quad i \neq j \end{aligned} \tag{13}$$

Recalling the separation of the in-plane variables from the thickness direction, employed for expressing the assumed displacement field as in Eq. (3), the bending, transverse normal and transverse shear components of the strains defined by Eq. (13) are recast in the following matrix notation

$$\boldsymbol{\epsilon}_b(x_\alpha, z_k) = \boldsymbol{Fb}_\tau(z_k)\, \boldsymbol{V}_\tau^{(k)}(x_\alpha); \tag{14a}$$

$$\boldsymbol{\epsilon}_n(x_\alpha, z_k) = \boldsymbol{Fn}_\tau(z_k)\, \boldsymbol{V}_\tau^{(k)}(x_\alpha); \tag{14b}$$

$$\boldsymbol{\epsilon}_s(x_\alpha, z_k) = \boldsymbol{Fs}_\tau(z_k)\, \boldsymbol{V}_\tau^{(k)}(x_\alpha) \tag{14c}$$

where $\boldsymbol{V}_\tau^{(k)}(x_\alpha)$ is the generalized strain vector of each layer defined as

$$\boldsymbol{V}_\tau^{(k)}(x_\alpha) = [\hat{u}_{1_\tau}^{(k)}\ \hat{u}_{1_{\tau,1}}^{(k)}\ \hat{u}_{1_{\tau,2}}^{(k)} \ \vdots\ \hat{u}_{2_\tau}^{(k)}\ \hat{u}_{2_{\tau,1}}^{(k)}\ \hat{u}_{2_{\tau,2}}^{(k)} \ \vdots\ \hat{u}_{3_\tau}^{(k)}\ \hat{u}_{3_{\tau,1}}^{(k)}\ \hat{u}_{3_{\tau,2}}^{(k)}\ ]^T \tag{15}$$

The explicit expressions for the matrices $\boldsymbol{Fb}_\tau$, $\boldsymbol{Fn}_\tau$ and $\boldsymbol{Fs}_\tau$ can be found in Eq. (A-1).

In order to introduce the transverse shear locking correction proposed in the next section, the transverse shear strain field given in Eq. (14c) is split into the classical $z-$ constant contribution $\boldsymbol{\gamma}^0$ of standard FSDT, and a contribution $\boldsymbol{\gamma}^h$ that depends on the thickness coordinate z and is related to high-order terms:

$$\boldsymbol{\epsilon}_s(x_\alpha, z_k) = \boldsymbol{\gamma}^0(x_\alpha) + \boldsymbol{\gamma}^h(x_\alpha, z_k) = \boldsymbol{Fs}_\tau^0\, \boldsymbol{V}_\tau^{(k)}(x_\alpha) + \boldsymbol{Fs}_\tau^{\boldsymbol{h}}(z_k)\, \boldsymbol{V}_\tau^{(k)}(x_\alpha) \tag{16}$$

Note that $\boldsymbol{Fs}_\tau^0$ is a matrix containing only constant values for all $z-$ dependency is contained in the matrix $\boldsymbol{Fs}_\tau^{\boldsymbol{h}}(z_k) = \boldsymbol{Fs}_\tau(z_k) - \boldsymbol{Fs}_\tau^0$. The matrices $\boldsymbol{Fs}_\tau^0$ for ESL and LW models of order N are reported explicitly in Eq. (A-2) and Eq. (A-3), respectively.

2.4. The two-dimensional weak form of the boundary value problem

The displacement field defined in Eq. (2) is inserted into the PVD Eq. (1) yielding the following expression

$$-\int_V \epsilon_{ij}(F_\tau \delta\hat{u}_{l_\tau})\, \sigma_{ij}(F_s \hat{u}_{m_s})\, \mathrm{d}x_i + \int_{\Gamma_\sigma} (\overline{F}_\tau \delta\hat{u}_{i_\tau})\, \bar{t}_i\, \mathrm{d}x_\alpha = 0 \tag{17}$$

where the summation indexes τ and s are used for the expansions of the virtual and the actual displacements, respectively, and $\overline{F}_\tau = F_\tau(\bar{z})$ are the thickness functions evaluated at the $\bar{z}-$ coordinate at which the external tractions $\bar{t}$ are applied. Taking into account the separation of the thickness direction from the in-plane variables, recalling the strain definitions in Eqs. (14) and expressing the layer-specific stresses through the constitutive law Eq. (12), the virtual internal work can be expressed in the following matrix form

$$\int_V \epsilon_{ij}(F_\tau \delta\hat{u}_{l_\tau})\, \sigma_{ij}(F_s \hat{u}_{m_s})\, \mathrm{d}x_i = \int_\Omega \sum_{k=1}^{N_L} \boldsymbol{V}_\tau^{(k)^T} \left\{ \int_{e^{(k)}} \begin{bmatrix} \boldsymbol{Fb}_\tau \\ \boldsymbol{Fn}_\tau \\ \boldsymbol{Fs}_\tau \end{bmatrix}^T \begin{bmatrix} \widetilde{\boldsymbol{C}}_{bb}^{(k)} & \widetilde{\boldsymbol{C}}_{bn}^{(k)} & \boldsymbol{0} \\ \widetilde{\boldsymbol{C}}_{bn}^{(k)^T} & \widetilde{\boldsymbol{C}}_{nn}^{(k)} & \boldsymbol{0} \\ \boldsymbol{0} & \boldsymbol{0} & \widetilde{\boldsymbol{C}}_{ss}^{(k)} \end{bmatrix} \begin{bmatrix} \boldsymbol{Fb}_s \\ \boldsymbol{Fn}_s \\ \boldsymbol{Fs}_s \end{bmatrix} \mathrm{d}z_k \right\} \boldsymbol{V}_s^{(k)}\, \mathrm{d}x_\alpha \tag{18}$$

The layer integrals along the thickness z_k are explicitly carried out according to the following notation

$$\begin{aligned} &\{\widetilde{\boldsymbol{Z}}_{bb_{\tau s}}^{(k)}, \widetilde{\boldsymbol{Z}}_{nb_{\tau s}}^{(k)}, \widetilde{\boldsymbol{Z}}_{bn_{\tau s}}^{(k)}, \widetilde{\boldsymbol{Z}}_{nn_{\tau s}}^{(k)}, \widetilde{\boldsymbol{Z}}_{ss_{\tau s}}^{(k)}\} \\ &\quad = \int_{e^{(k)}} \{\boldsymbol{Fb}_\tau^T \widetilde{\boldsymbol{C}}_{bb}^{(k)} \boldsymbol{Fb}_s,\ \boldsymbol{Fb}_\tau^T \widetilde{\boldsymbol{C}}_{bn}^{(k)} \boldsymbol{Fn}_s,\ \boldsymbol{Fn}_\tau^T \widetilde{\boldsymbol{C}}_{nb}^{(k)} \boldsymbol{Fb}_s, \\ &\qquad \boldsymbol{Fn}_\tau^T \widetilde{\boldsymbol{C}}_{nn}^{(k)} \boldsymbol{Fn}_s,\ \boldsymbol{Fs}_\tau^T \widetilde{\boldsymbol{C}}_{ss}^{(k)} \boldsymbol{Fs}_s\}\, \mathrm{d}z_k \end{aligned} \tag{19}$$

Furthermore, the special treatment of the transverse shear strain given in Eq. (16) is introduced, which yields to the following subdivision

$$\widetilde{\boldsymbol{Z}}_{ss_{\tau s}}^{(k)} = \widetilde{\boldsymbol{Z}}_{ss_{\tau s}}^{00(k)} + \widetilde{\boldsymbol{Z}}_{ss_{\tau s}}^{0\,h(k)} + \widetilde{\boldsymbol{Z}}_{ss_{\tau s}}^{h0(k)} + \widetilde{\boldsymbol{Z}}_{ss_{\tau s}}^{hh(k)} \tag{20}$$

This permits to identify those terms that involve the $z-$ constant transverse shear strains responsible of the locking phenomenon.

The two-dimensional matrix expression for the virtual internal work is finally written as

$$\begin{aligned} &\int_V \epsilon_{ij}(F_\tau \delta\hat{u}_{l_\tau})\, \sigma_{ij}(F_s \hat{u}_{m_s})\, \mathrm{d}x_i \\ &\quad = \int_\Omega \left\{ \sum_{k=1}^{N_L} \boldsymbol{V}_\tau^{(k)^T} [\widetilde{\boldsymbol{Z}}_{bb_{\tau s}}^{(k)} + \widetilde{\boldsymbol{Z}}_{bn_{\tau s}}^{(k)} + \widetilde{\boldsymbol{Z}}_{nb_{\tau s}}^{(k)} + \widetilde{\boldsymbol{Z}}_{nn_{\tau s}}^{(k)} + \widetilde{\boldsymbol{Z}}_{ss_{\tau s}}^{hh(k)} + \widetilde{\boldsymbol{Z}}_{ss_{\tau s}}^{0\,h(k)} \right. \\ &\qquad \left. + \widetilde{\boldsymbol{Z}}_{ss_{\tau s}}^{h0(k)} + \widetilde{\boldsymbol{Z}}_{ss_{\tau s}}^{00(k)}] \boldsymbol{V}_s^{(k)} \right\} \mathrm{d}x_\alpha \end{aligned} \tag{21}$$

The terms in Eq. (17) related to external tractions are developed in a similar manner; details can be found elsewhere [24,23] and are here omitted for brevity.

3. Finite element approximations

The solution of the two-dimensional boundary value problem expressed in the previous section is sought in weak form according to the finite element (FE) method. This section presents the four-node quadrilateral FE approximation and details out the new QC4 approximation for avoiding transverse shear locking problems and minimizing the convergence rate loss for distorted meshes.

3.1. Approximation for the geometry

The physical domain (x_1, x_2) is mapped onto the reference, bi-unit square element, defined by the natural non-dimensional coordinates (ξ, η), through to the bilinear Lagrange interpolation functions $N(\xi, \eta)$:

$$x_\alpha = N_i(\xi, \eta) X_{\alpha_i} \quad (i = 1, \ldots 4) \tag{22}$$

where X_{α_i} are the $x_\alpha-$ coordinates of the four corner nodes, see Fig. 2.

3.2. Isoparametric interpolation

According to the isoparametric approach, the same interpolation defined by Eq. (22) is employed for approximating the unknown functions and their in-plane derivatives contained in $\boldsymbol{V}_\tau^{(k)}(x_\alpha)$:

$$\boldsymbol{V}_\tau^{(k)} = \boldsymbol{B}_{\tau\, i} \boldsymbol{q}_{\tau\, i}^{(k)} \quad (i = 1, \ldots 4) \tag{23}$$

where $\boldsymbol{q}_{\tau\, i}^{(k)} = [u_{1_\tau}^{(k)}\ u_{2_\tau}^{(k)}\ u_{3_\tau}^{(k)}]_i^T$ is the DOF vector of the node i related to the layer k and the expansion order index τ. The 9×3 matrix $\boldsymbol{B}_{\tau\, i}$

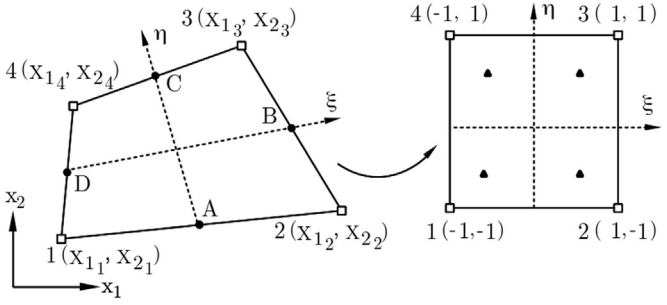

Fig. 2. Four-node quadrangular element in the physical frame x_1, x_2 and natural frame ξ, η.

.

contains the shape functions $N_i(\xi, \eta)$ of Eq. (22) and their derivatives with respect to the physical coordinates x_α. Introducing the FE approximation Eq. (23) into Eq. (21) yields the definition of the 3×3 *fundamental nucleus* of the classical CUF-based plate elements

$$\boldsymbol{K}_{ij\,\tau s}^{(k)} = \int_\Omega \boldsymbol{B}_{\tau\,i}^T [\widetilde{\boldsymbol{Z}}_{bb_{\tau s}}^{(k)} + \widetilde{\boldsymbol{Z}}_{nb_{\tau s}}^{(k)} + \widetilde{\boldsymbol{Z}}_{bn_{\tau s}}^{(k)} + \widetilde{\boldsymbol{Z}}_{nn_{\tau s}}^{(k)} + \widetilde{\boldsymbol{Z}}_{ss_{\tau s}}^{(k)}] \boldsymbol{B}_{s\,j}\, \mathrm{d}x_\alpha \tag{24}$$

Explicit expressions of this model-invariant kernel can be found in several works [24,23]. These references report also the expansion procedure over the summation indexes τ and s as well as the assembly of all layers k, which are here omitted for brevity.

For the present four-node element, a 2×2 Gauss quadrature scheme is employed for an exact numerical evaluation of the domain integral (the 4 Gauss points are represented by the black triangles in Fig. 2). In order to contrast the shear locking phenomenon, the transverse shear stiffness contribution related to $\widetilde{\boldsymbol{Z}}_{ss_{\tau s}}^{(k)}$ has been reduced-integrated [24] or treated within a MITC approach [41]. In this work, however, a new interpolation for the $z-$ constant transverse shear strain is presented, which affects only the contributions $\widetilde{\boldsymbol{Z}}_{ss}^{00}$, $\widetilde{\boldsymbol{Z}}_{ss}^{h0}$ and $\widetilde{\boldsymbol{Z}}_{ss}^{0\,h}$.

3.3. The new QC4 interpolation

The isoparametric interpolation for the transverse shear field leads to a locking phenomenon because of the incompatibility of the polynomial spaces defined by the sum of $\hat{u}_{\alpha_\tau}$ and the in-plane derivative $\hat{u}_{3_{\tau,\alpha}}$ ($\alpha = 1, 2$ for γ_{13}^0 and γ_{23}^0, respectively) [16]. The locking pathology is associated to the $z-$ constant part only, for higher-order contributions depend on the plate thickness and vanish naturally in the thin plate limit. Thus a new, field-compatible interpolation for the four-node element is constructed for the $z-$ constant part $\boldsymbol{\gamma}^0$: this is an extension to arbitrary variable kinematics plate models of the approach proposed in [47] for FSDT plate elements and in [16] to a refined plate element. The new interpolation is constructed as follows:

- In order to enhance the element's robustness for distorted shapes, the $z-$ constant part of transverse shear strain components is first written in the element's natural coordinate system (ξ, η) as:

$$\begin{bmatrix} \gamma_\xi^0(\xi,\eta) \\ \gamma_\eta^0(\xi,\eta) \end{bmatrix}^{(k)} = \boldsymbol{Fs}_\tau^0\, \boldsymbol{U}_\tau^{(k)}(\xi,\eta) \tag{25}$$

  where

$$\boldsymbol{U}_\tau^{(k)}(\xi,\eta) = \left[\hat{u}_{\xi_\tau}^{(k)}\ \hat{u}_{\xi_{\tau,\xi}}^{(k)}\ \hat{u}_{\xi_{\tau,\eta}}^{(k)} \vdots \hat{u}_{\eta_\tau}^{(k)}\ \hat{u}_{\eta_{\tau,\xi}}^{(k)}\ \hat{u}_{\eta_{\tau,\eta}}^{(k)} \vdots \hat{u}_{3_\tau}^{(k)}\ \hat{u}_{3_{\tau,\xi}}^{(k)}\ \hat{u}_{3_{\tau,\eta}}^{(k)} \right]^T \tag{26}$$

  is the projection onto the reduced natural coordinates ξ, η of the generalized strain vector $\boldsymbol{V}_\tau^{(k)}$.
- The field-compatible approximation shall be constructed upon enhancing the polynomial space of the transverse deflection $\hat{u}_{3_\tau}^{(k)}$ so that its derivative matches the bi-linear space of the in-plane displacements $\hat{u}_{\xi_\tau}$ and $\hat{u}_{\eta_\tau}$. For this, a quadratic serendipity interpolation is assumed for $\hat{u}_{3_\tau}^{(k)}$ by introducing four supplementary DOFs, $(\hat{u}_{3_{\tau,\xi}})_A$, $(\hat{u}_{3_{\tau,\eta}})_B$, $(\hat{u}_{3_{\tau,\xi}})_C$ and $(\hat{u}_{3_{\tau,\eta}})_D$, at the mid-side points, see Fig. 2. The supplementary DOFs are subsequently expressed in terms of the DOFs at the four corner nodes by imposing the tangential component of the transverse shear strain to be constant along the element's edges, viz.

$$\gamma_\xi^0(\xi, \eta = \pm 1) = \text{constant}; \quad \gamma_\eta^0(\xi = \pm 1, \eta) = \text{constant} \tag{27}$$

  A new interpolation for the transverse deflection $\hat{u}_{3_\tau}$ is thus obtained through these four equations. The resulting four-node FE shall be denoted QC4 due to the quadratic and constant approximations employed for the transverse deflection and the tangential transverse shear strain, respectively.
- The new field-compatible interpolation for γ_ξ^0, γ_η^0 is defined by the polynomial basis obtained from the intersection sets of monomial terms in ξ and η:

$$\begin{aligned} \mathcal{B}(\gamma_\xi^0) &= \mathcal{B}(u_{\xi_\tau}) + \mathcal{B}(u_{3_{\tau,\xi}}) = \{1, \eta\} \\ \mathcal{B}(\gamma_\eta^0) &= \mathcal{B}(u_{\eta_\tau}) + \mathcal{B}(u_{3_{\tau,\eta}}) = \{1, \xi\} \end{aligned} \tag{28}$$

- According to the polynomial basis spanning the transverse shear strain components, only two points are required for defining the resulting linear variations along the reduced natural coordinates. Choosing these points to be the four mid-side points $A-D$ (see Fig. 2), one has

$$\begin{aligned} \gamma_\xi^0(\xi,\eta) &= C_{\xi 1}(\xi,\eta)\, \gamma_\xi^0(\xi_A,\eta_A) + C_{\xi 2}(\xi,\eta)\, \gamma_\xi^0(\xi_C,\eta_C) \\ \gamma_\eta^0(\xi,\eta) &= C_{\eta 1}(\xi,\eta)\, \gamma_\eta^0(\xi_D,\eta_D) + C_{\eta 2}(\xi,\eta)\, \gamma_\eta^0(\xi_D,\eta_D) \end{aligned} \tag{29a}$$

  with the following interpolating functions:

$$\begin{aligned} C\xi_1(\xi,\eta) &= \frac{(1-\eta)}{2}; \quad C\xi_2(\xi,\eta) = \frac{(1+\eta)}{2} \\ C\eta_1(\xi,\eta) &= \frac{(1-\xi)}{2}; \quad C\eta_2(\xi,\eta) = \frac{(1+\xi)}{2} \end{aligned} \tag{29b}$$

- The physical transverse shear strains are finally deduced from the transverse shear strains in the reference domain as

$$\begin{bmatrix} \gamma_{13}^0(\xi,\eta) \\ \gamma_{23}^0(\xi,\eta) \end{bmatrix} = \boldsymbol{J}^{-1} \begin{bmatrix} \gamma_\xi^0(\xi,\eta) \\ \gamma_\eta^0(\xi,\eta) \end{bmatrix} \tag{30}$$

  where the $\boldsymbol{J}$ is the 2×2 Jacobian matrix evaluated at the 4 Gauss points used for integrating the stiffness matrix.

The expression for the QC4 approximation for the $z-$ constant transverse shear strain field can be finally written as

$$\boldsymbol{\gamma}^0 = \boldsymbol{J}^{-1}\, \boldsymbol{Fs}_\tau^0\, \overline{\boldsymbol{B}}_i\, \boldsymbol{q}_{\tau\,i}^{(k)} \tag{31}$$

where $\overline{\boldsymbol{B}}_i$ is the matrix containing the modified QC4 interpolation functions and their derivatives with respect to the physical coordinates x_α. The explicit expression of the four $\overline{\boldsymbol{B}}_i$ matrices is given in Eq. (A-4).

4. Numerical results

Several numerical benchmark problems are considered for displaying the accuracy and robustness of the proposed QC4 CUF-based plate element. The classical CUF acronyms are used for naming the various plate models: the polynomial order N is appended to a string that identifies whether the model is ESL (EDN), Zig-Zag (EDZN) or LW (LDN).

A first set of problems involving a simple homogeneous and isotropic plate is used for assessing the element's performance, i.e., the properties of the stiffness matrix via an eigenvalue analysis, the convergence rate for thin and thick plates, and the sensitivity with respect to distorted element shapes; these latter tests are conducted on a square plate with distorted mesh, a skew plate and a circular plate. Previous analyses have shown that all CUF-based elements have the same sensitivity to shear locking irrespective of the order of expansion N [40]. The case studies considered in this first problem set are hence computed with the ED2 model only, an ESL model that retains the three-dimensional constitutive law without Poisson locking.

A final set of problems is subsequently proposed for demonstrating the accuracy of the predicted displacements and stresses for homogeneous and composite, thin and thick plates. In this latter case study, several CUF-based elements are used for highlighting the variable kinematics framework.

The influence of the boundary conditions and type of loading are

Table 1
Acronyms for boundary conditions and type of loading.

Boundary conditions		Loading	
(SA)	Simply supported	(P)	Uniform load q_0 at top surface
(CL)	Clamped	(C)	Concentrated force $\overline{P}$ at plate center

also addressed; Table 1 lists the acronyms used for denoting the various configurations. For all tests except the skew plate, symmetry is exploited to reduce the model to only a quarter plate.

Present QC4 results are compared against solutions obtained with the following isoparametric approaches:

ISO full-integrated isoparametric element(2×2 Gauss points for the whole stiffness matrix)
ISO-SI isoparametric element with selective integration(1 Gauss point for transverse shear stiffness contributions)

All elements are implemented as user subroutines into the commercial ABAQUS software. A dedicated pre-processing tool allows to prepare the FE model within the ABAQUS/CAE graphical interface.

4.1. The properties of the stiffness matrix

The eigenvalues of the stiffness matrix of a square element are analyzed for a thin and a thick plate, according to the following configuration

geometry square element $a \times a$ (a=1), thickness $e = 10^{-n}$ (n = 1, 3)
boundary conditions (SA)
material properties isotropic with E=10.92 and $\nu = 0.3$

The results of the eigenvalue analysis are reported for thick and thin plates in Figs. 3 and 4, respectively. The proposed graphics allow to recognize at a glance the eigenvalues associated to rigid-body modes as well as the gap between them and those associated to deformation modes. It is apparent that the proposed QC4 element and the full-integrated isoparametric element have the correct number of rigid-body modes, i.e., 6, regardless of the element's slenderness S=a/e. On the contrary, the selective reduced integration scheme entails 3 spurious zero-energy modes, which indicates the possibility of an unstable behavior of both, thick and thin elements.

4.2. The transverse shear locking

A numerical test is carried out to assess the sensitivity of the proposed QC4 element to the transverse shear locking. The test is described as follows:

geometry square plate $a \times a$ (a=1), thickness $e = 10^{-n}$ with $n \in \{0, 4\}$
boundary conditions (SA) or (CL) on all sides
loading (P) or (C)
material properties isotropic with E=10.92 and $\nu = 0.3$
mesh regular with N = 2, 4, 8, 16, 32 (see Fig. 5)
results transverse displacement U_3 at the center of the plate

reference values Kirchhoff-Love theory $\left(D = \frac{E}{12(1-\nu^2)}\right)$ [51]:**(SA-P)**

$$U_3^a(a/2,\ a/2,\ 0) = 0.00406\ q_0\ \frac{a^4}{e^3\ D}\ \textbf{(CL-P)}$$

$$U_3^a(a/2,\ a/2,\ 0) = 0.00126\ q_0\ \frac{a^4}{e^3\ D}\ \textbf{(SA-C)}$$

$$U_3^a(a/2,\ a/2,\ 0) = 0.0116\ \overline{P}\ \frac{a^2}{e^3\ D}\ \textbf{(CL-C)}$$

$$U_3^a(a/2,\ a/2,\ 0) = 0.0056\ \overline{P}\ \frac{a^2}{e^3\ D}$$

Four configurations are considered, defined by the combination of boundary conditions and loading. The concentrated force is applied only to thin plates with $S \geq 10^2$ in order to avoid the singularity at the loaded node; thick plates (S=10) are considered only for a uniform pressure loading. In view of an assessment of the sensitivity to the transverse shear locking, the results are summarized in two different ways:

- *Constant mesh, varying slenderness ratio*
  Three regular meshes with N = 4, 8, 16 have been considered for the quarter plate (see Fig. 5) and, for each mesh, the results are given for varying length-to-thickness ratios S=a/e: Figs. 6 and 7 report the results for plates subjected to a uniform pressure load and a concentrated force, respectively. For both loading types, the full-integrated isoparametric element is shown to suffer a very strong locking as the plate becomes thin ($S \geq 10^2$). On the contrary, both the QC4 and the ISO-SI elements are free from transverse shear locking and provide the reference Kirchhoff-Love values with good accuracy: a N=8 mesh is sufficient to obtain accurate results for all configurations.
- *Convergence analysis for a thin or thick plate*
  The convergence curves of the transverse displacement at the plate's center with respect to the mesh density are shown in log-log scale in Fig. 8 and 9 for various length-to-thickness ratios (S = 10, 10^2, 10^4). The previous comments are confirmed: the convergence rate of the full-integrated ISO element is shown to strongly degrade as the length-to-thickness ratio S increases, a behavior that clearly indicates the presence of the transverse shear locking pathology; on the contrary, the convergence rate of the QC4 and ISO-SI elements remains sensibly the same irrespective of the length-to-thickness ratio. The monotone convergence of the QC4 element can be appreciated. As expected, the accuracy of the results depends on the test case for a given mesh.

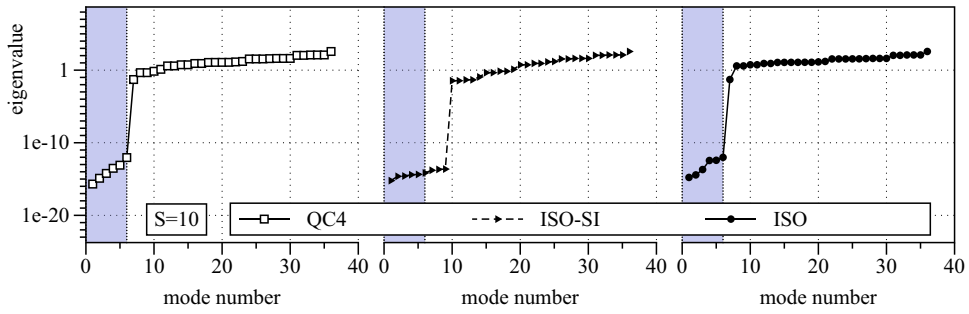

Fig. 3. Eigenvalues of the stiffness matrix for an ED2 model and thick plate (a/e = 10).

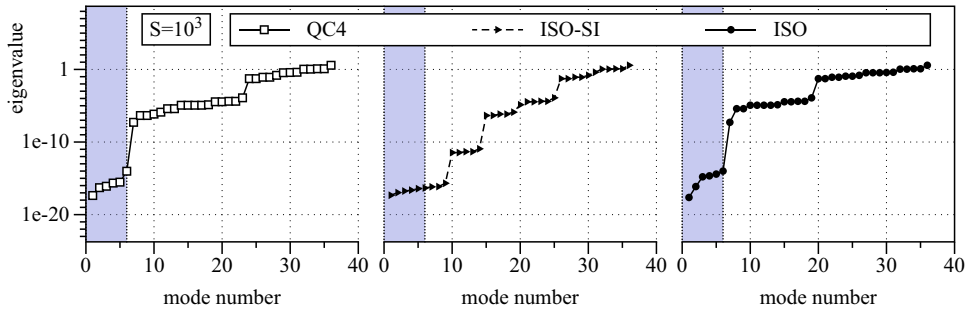

Fig. 4. Eigenvalues of the stiffness matrix for an ED2 model and thin plate ($a/e = 10^3$).

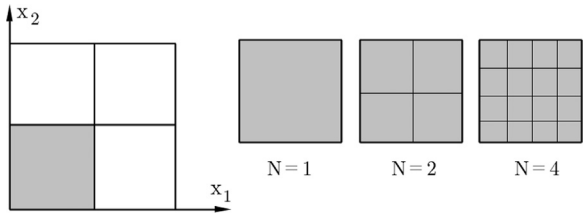

Fig. 5. Regular meshes for a quarter of the plate.

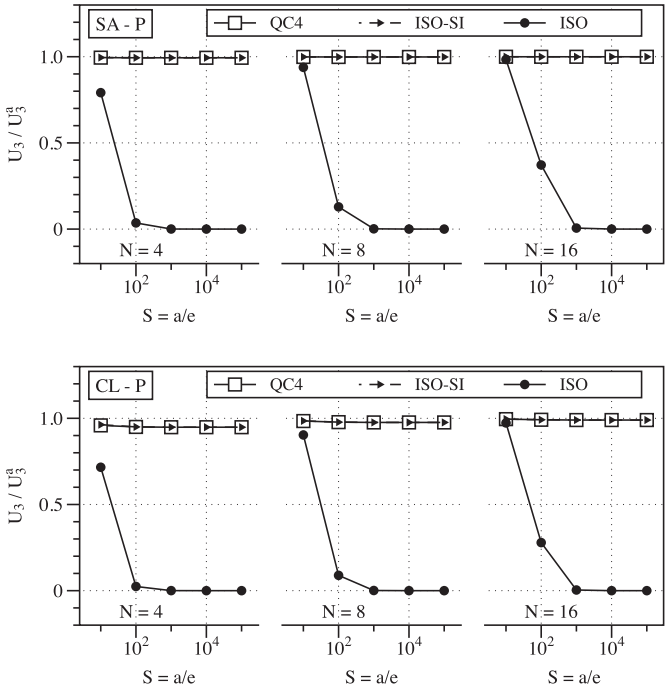

Fig. 6. Transverse displacement with respect to slenderness ratio for thick (S=10) to very thin plates ($S = 10^5$) under a pressure load.

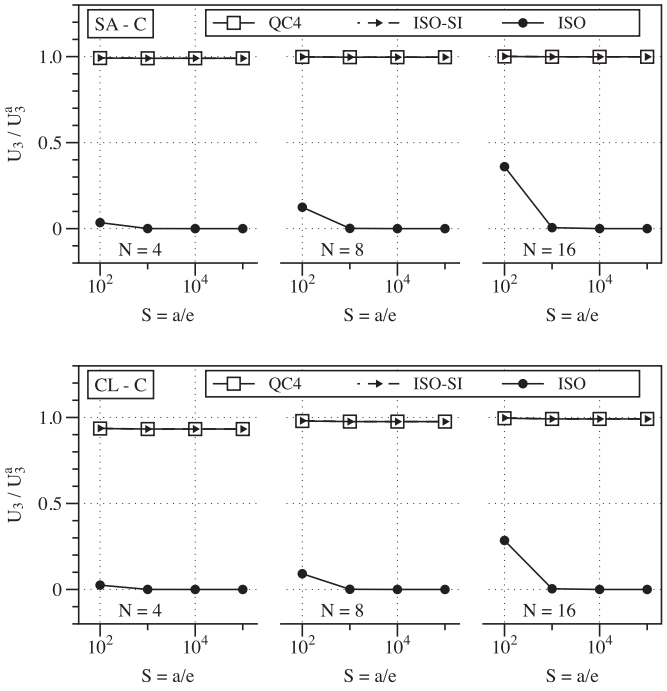

Fig. 7. Transverse displacement with respect to slenderness ratio for thin plates ($S \geq 10^2$) under a concentrated load.

4.3. The distortion tests

In this section, the sensitivity of the present FE to the mesh distortion is illustrated on three test cases widely used in open literature, namely the square, skew and circular plate.

4.3.1. The square plate test

This standard test is classically used in order to investigate the mesh sensitivity in plate bending problems. The data are given as follows:

geometry square plate $a \times a$ with $a = 100$ and thickness $e = 0.1$
boundary conditions (SA) or (CL) on all sides
loading (P) or (C)
material properties isotropic with $E = 10.92$ and $\nu = 0.3$
mesh $N = 2$ for the quarter plate, with the distortion parameter $s \in \{-12, -8, -4, 0, 4, 8, 12\}$ (see Fig. 10)
results transverse displacement $U_3 = u_3(a/2, a/2, 0)$ at plate's center
reference value transverse displacement $U_3^{(0)}$ for the regular mesh (s=0)

In this test, the distorted meshes are characterized by the parameter s defining the coordinates of the mid-node of the quarter plate, which is located in the undistorted mesh (s=0) at $X_1 = X_2 = a/4$. The parameter s may be positive or negative, as illustrated in Fig. 10, and defines the coordinates of the mid-node as $(a/4 + s, a/4 + s)$: for the most distorted meshes ($s = \pm 12$) the mid-node is hence located at $(\pm 37, \pm 37)$. Note that it is not usual in open literature to consider positive and negative values for the parameter s.

The transverse displacement U_3 at the center node is normalized with respect to the value U_3^0 obtained with the regular, undistorted mesh (s=0). Fig. 11 shows the results obtained by the QC4, ISO and ISO-SI elements with ED2 kinematics for the four configurations defined by combining the two boundary and loading conditions. As expected, the largest errors occur for the most distorted meshes. The maximum absolute errors occurring for the four configurations are summarized in Table 2. The results indicate that QC4 is the most robust element with respect to mesh distortion for all boundary

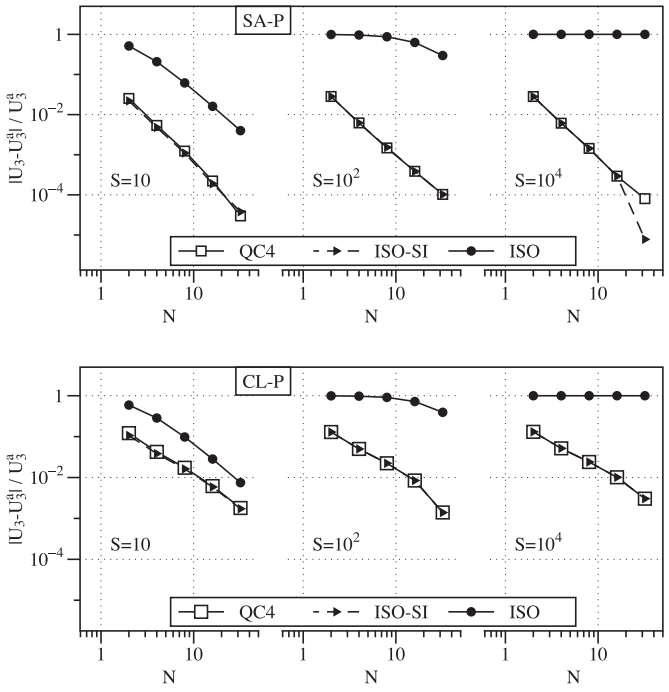

Fig. 8. Convergence of the transverse displacement for thick (S=10) and thin ($S = 10^2, 10^4$) plates under a pressure load.

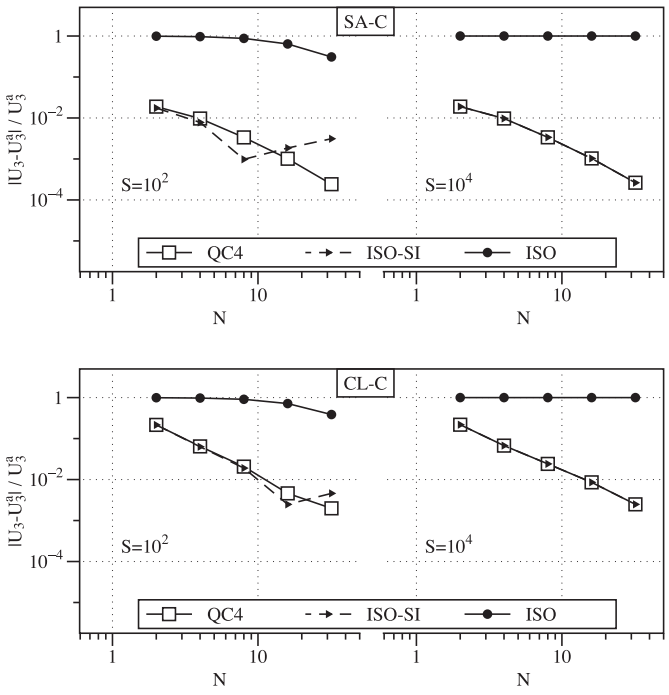

Fig. 9. Convergence of the transverse displacement for thin plates ($S = 10^2, 10^4$) under a concentrated load.

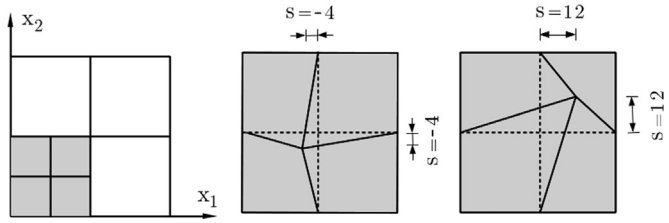

Fig. 10. Meshes for the quarter plate with distortion defined by the parameter s.

conditions, with a maximum error that does not exceed 20%. The highest distortion sensitivity is displayed by the full-integrated ISO element.

4.3.2. Razzaque's skew plate test

This benchmark originally proposed by Razzaque [52] is illustrated in Fig. 12 and defined by the following data:

geometry skewed square plate $a \times a$ with $a = 100$ and thickness $e = 0.1$, skew angle $\psi = 60°$
boundary conditions (SA) on straight edges, oblique edges are free
loading (P)
material properties isotropic with $E = 10^3$ and $\nu = 0.31$
mesh $N = 2, 4, 8, 16, 32, 64$ skew elements for whole plate
results non-dimensional transverse deflection at plate's center:

$$\overline{U}_3 = u_3(0, 0, 0)\frac{10^2 D}{q_0 a^4} \text{ with } D = \frac{E}{12(1-\nu^2)}$$

reference value $\overline{U}_3 = 0.7945$ (from [52])

Table 3 reports the non-dimensional transverse displacement at the center of the skew plate, obtained by the QC4, ISO-SI and ISO elements with ED2 kinematics for different mesh densities N. The table also reports the percentage errors with respect to Razzaque's reference solution, which allows to identify the convergence rate of the three elements: the ISO-SI and QC4 elements show the same convergence rate and recover the reference solution with approximately 1% error with a N=16 mesh. The ISO element yields very poor results as a consequence of two causes, namely the severe transverse shear locking affecting the response of the thin plate ($S = a/e = 10^3$) and the high sensitivity to non-rectangular element shapes. This test thus confirms the robustness of the present QC4 element.

4.3.3. The circular plate test

A last mesh distortion sensitivity test is considered, which concerns the bending of a clamped circular isotropic plate subjected to a uniform pressure load according to the following data:

geometry circular plate of radius $R = 5$ and thickness $e = 0.1$
boundary conditions (CL) on the external perimeter
loading (P)
material properties isotropic with $E = 1.7472\ 10^7$ and $\nu = 0.3$
mesh $N = 3, 12, 28, 60$ elements for a quarter plate (see Fig. 13)
results deflection $U_3 = u_3(0, 0, 0)$ at the center of the plate
reference value Kirchhoff-Love theory $U_3^{\text{ref}} = 0.61147\ 10^{-6}$ [53]

The evolution of the ratio between the central deflection and the Kirchhoff-Love solution with respect to the mesh density is reported in Fig. 14. The convergence is compared for the QC4, ISO and ISO-SI elements with ED2 kinematics. As previously discussed, the ISO element suffers the distorted shapes and for the present case it shows errors exceeding 90% even with the more refined mesh. It can be noticed that the QC4 element has a good convergence rate and its accuracy is very satisfactory. In particular, the error becomes less than 3% for $N \geq 30$, whereas the converged result of the ISO-SI FE is still affected with an error of about 10%.

4.4. Mechanical analysis of isotropic plates

The focus is here set on the convergence of displacement and stresses predicted by the proposed QC4 element for a plate bending problem. The benchmark problem is defined as follows:

geometry square plate $a \times a$ and length-to-thickness ratio

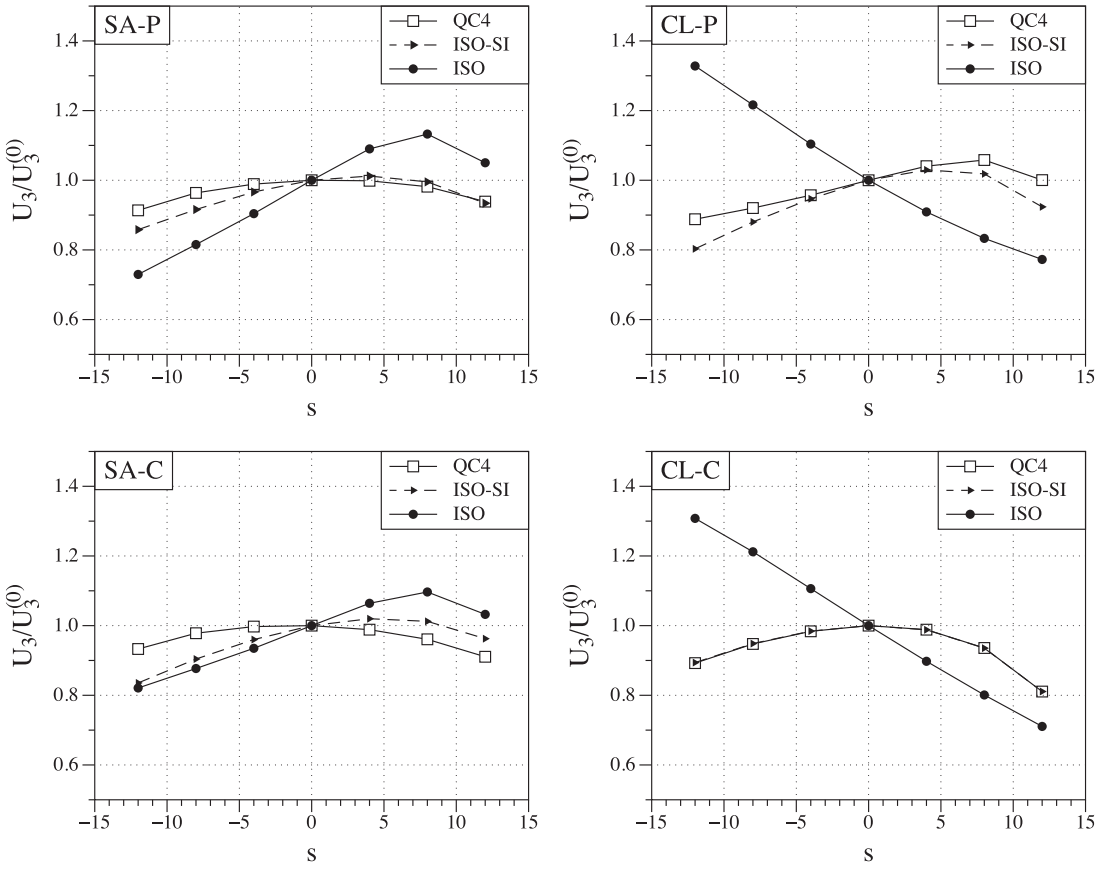

Fig. 11. Variation of the normalized central deflection with respect to the parameter s for square plates with various loading and boundary conditions (ED2 model).

Table 2
Maximum absolute error of the central deflection and corresponding $s-$ value for various boundary and loading conditions.

Config.	QC4		ISO-SI		ISO	
	error [%]	s	error [%]	s	error [%]	s
SA-P	8.6	−12	14.2	−12	27.0	−12
SA-C	8.9	+12	16.5	−12	17.9	−12
CL-P	11.2	−12	19.7	−12	32.8	−12
CL-C	18.9	+12	18.9	+12	30.8	+12

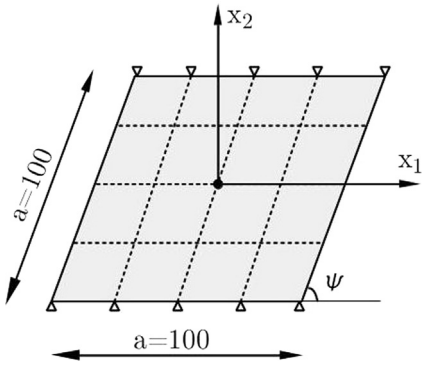

Fig. 12. Razzaque's skew plate test (mesh N=4).

$$S = \frac{a}{e} = 2,\ 5,\ 10,\ 100$$

boundary conditions (SA)
loading bi-sinusoidal pressure on the top surface:

Table 3
Non-dimensional deflection at the center point of Razzaque's skew plate (values in parentheses are the percentage errors with respect to the reference solution).

S	N=2	N=4	N=8	N=16	N=32	N=64
ISO	0.0000 *(−100.0%)*	0.0000 *(−100.0%)*	0.0002 *(−100.0%)*	0.0007 *(−99.9%)*	0.0029 *(−99.6%)*	0.0114 *(−98.6%)*
ISO–SI	0.3269 *(−58.9%)*	0.6616 *(−16.7%)*	0.7547 *(−5.0%)*	0.7843 *(−1.3%)*	0.7908 *(−0.5%)*	0.7927 *(−0.2%)*
QC4	0.3727 *(−53.1%)*	0.6609 *(−16.8%)*	0.7533 *(−5.2%)*	0.7838 *(−1.3%)*	0.7908 *(−0.5%)*	0.7927 *(−0.2%)*

$$q_3(x_1, x_2, z = e/2) = q_0 \sin\left(\frac{\pi x}{a}\right) \sin\left(\frac{\pi x_2}{a}\right)$$

material properties isotropic with E=73 GPa and $\nu = 0.34$
results non-dimensional response defined as

$$\overline{U}_1 = u_1(0, a/2, -e/2)\frac{E}{q_0 e S^3}$$

$$\overline{U}_3 = u_3(a/2, a/2, 0)\frac{100E}{q_0 e S^4}$$

$$\overline{\sigma}_{11} = \sigma_{11}(a/2, a/2, e/2)\frac{1}{q_0 S^2}$$

$$\overline{\sigma}_{13} = \sigma_{13}(0, a/2, 0)\frac{1}{q_0 S}$$

reference value closed-form Navier-type solution (ED2 model)

The convergence behavior for displacements and stresses of the QC4 element is reported in Fig. 15, where both very thick (S=5) and thin (S=100) plates are considered. The present results are obtained with an ED2 kinematics and the FE error is defined with respect to the closed-form

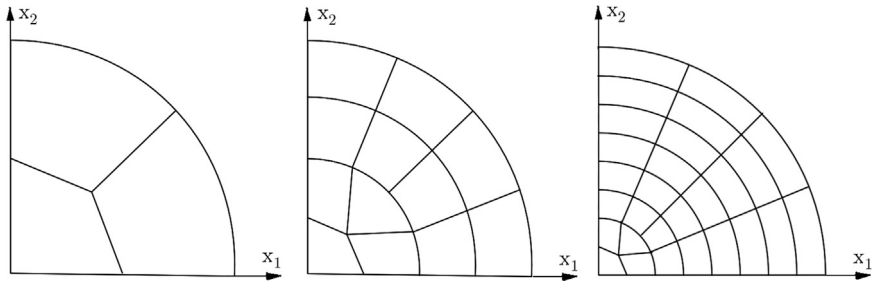

Fig. 13. FE meshes with N = 3, 12, 28 elements of a quarter of the circular plate.

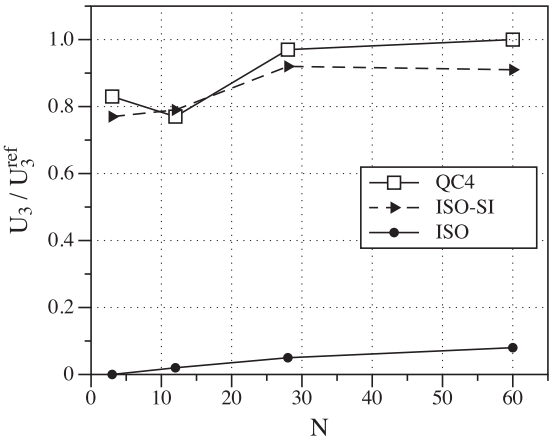

Fig. 14. Convergence study of the central deflection for the circular plate.

Navier-type solutions obtained with the same ED2 model. The convergence rate is shown to be independent of the length-to-thickness ratio and is very good for both, displacements and stresses: note that all discretization errors are less than 1% if a mesh with $N \geq 8$ elements is used.

Fig. 16 displays the distributions along the $z-$ axis of the normalized transverse stresses $\bar{\sigma}_{13}(z) = \sigma_{13}(0, a/2, z)/(q_0 S)$ and $\bar{\sigma}_{33}(z) = \sigma_{33}(a/2, a/2, z)/q_0$, computed directly from the constitutive equations, when the plate thickness is subdivided into $N_L = 1, 3, 5$ numerical layers with an LD4 kinematics. A FE mesh with N=8 has been used for the results in Fig. 16. It is shown that, for the present case of isotropic plate, the refinement of the response across the thickness by means of numerical layers has no effect and the converged solution is reached with N_L=1. For a thick plate (S=5), the LD4 model is capable to accurately recover the natural boundary conditions at the outer surfaces of the plate, see Fig. 16 (left). In case of a thin plate (S=100), however, the transverse normal stress distribution is highly inaccurate, see Fig. 16 (right). Fig. 17 shows that, for a thin plate, it is necessary to refine the in-plane FE mesh in order to enhance the accuracy of the σ_{33} distribution across the thickness, up to the fulfillment of the natural boundary conditions at the outer surfaces of the plate, see also [16].

4.5. Mechanical analysis of laminated composite plates

This final case study involves simply-supported cross-ply laminates subjected to a bi-sinusoidal pressure load, for which Pagano provided exact elasticity results [54]. The following configuration is considered:

geometry square plate $a \times a$ and length-to-thickness ratio $S = \dfrac{a}{e} = 4, 10, 100$

boundary conditions (SA)

loading bi-sinusoidal pressure on the top surface:-

$$q_3(x_1, x_2, z = e/2) = q_0 \sin\left(\frac{\pi x}{a}\right) \sin\left(\frac{\pi x_2}{a}\right)$$

material properties three-layered cross-ply plate (0°/90°/0°); each layer has thickness $e^{(k)} = e/3$ and orthotropic properties: $E_L/E_T = 25$; $G_{LT}/E_T = 0.5$; $G_{TT}/E_T = 0.2$; $\nu_{LT} = \nu_{TT} = 0.25$ (L, T indicate longitudinal and transverse directions, respectively)

mesh N=8 for the quarter plate

results displacements and stresses are made non-dimensional according to

$$\begin{aligned}
\bar{u}_\alpha &= u_\alpha \frac{E_T}{q_0 e S^3} \text{for} \begin{cases} u_1(0, a/2, z) \\ u_2(a/2, 0, z) \end{cases} \\
\bar{u}_3 &= u_3(a/2, a/2, z) \frac{100 E_T}{q_0 e S^4} \\
\bar{\sigma}_{\alpha\beta} &= \sigma_{\alpha\beta} \frac{1}{q_0 S^2} \text{for} \begin{cases} \sigma_{11}(a/2, a/2, z) \\ \sigma_{22}(a/2, a/2, z) \\ \sigma_{12}(0, 0, z) \end{cases} \\
\bar{\sigma}_{\alpha 3} &= \sigma_{\alpha 3} \frac{1}{q_0 S} \text{for} \begin{cases} \sigma_{13}(0, a/2, z) \\ \sigma_{23}(a/2, 0, z) \end{cases} \\
\bar{\sigma}_{33} &= \sigma_{33}(a/2, a/2, z) \frac{1}{q_0}
\end{aligned}$$

reference value 3D exact elasticity results given by Pagano [54]

Three ESL models (ED2, ED4 and EDZ4) and two LW models (LD2 and LD4) are considered in order to assess different plate theories. Present QC4 results, identified by the suffix *-FEM*, are compared

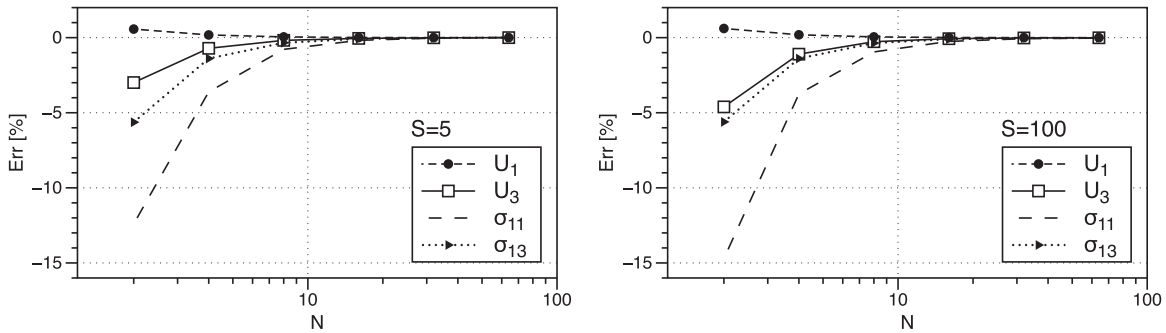

Fig. 15. Simply-supported square isotropic plate under bi-sinusoidal pressure load: convergence of displacements and stresses with respect to corresponding closed-form solutions (ED2 model) for length-to-thickness ratios S=5 (left) and S=100 (right).

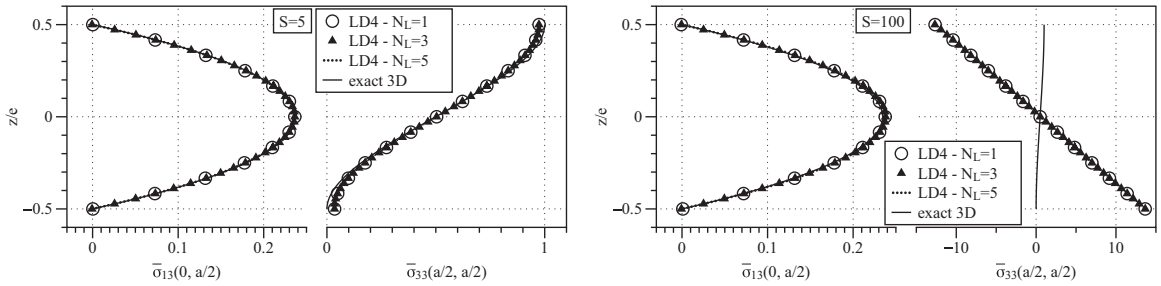

Fig. 16. Influence of the number of numerical layers N_L on the through-thickness distribution of $\bar{\sigma}_{13}$ and $\bar{\sigma}_{33}$ for a thick (S=5, left) and a thin (S=100, right) plate (isotropic plate loaded at top surface, LD4, N=8).

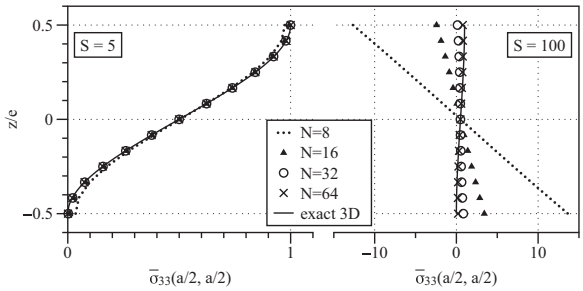

Fig. 17. Influence of the FE mesh on the through-thickness distribution of the $\bar{\sigma}_{33}$ (isotropic plate loaded at top surface, LD4, N_L=1).

Table 4
Simply-supported (0°/90°/0°) square plate under bi-sinusoidal pressure load: Non-dimensional displacements for length-to-thickness ratios S = 4, 10, 100.

S	Model	$\bar{u}_1\left(-\frac{e}{2}\right)$	$\bar{u}_2\left(-\frac{e}{2}\right)$	$\bar{u}_3(0)$
4	**Ref. [54]**	**0.0094**	**0.0228**	**2.0059**
	ED2-anlt	0.0052 *(44.43%)*	0.0164 *(28.00%)*	1.5440 *(23.03%)*
	ED2-FEM	0.0052 *(44.48%)*	0.0165 *(27.83%)*	1.5457 *(22.94%)*
	ED4-anlt	0.0092 *(1.93%)*	0.0216 *(5.03%)*	1.8926 *(5.65%)*
	ED4-FEM	0.0092 *(2.09%)*	0.0217 *(4.93%)*	1.8920 *(5.68%)*
	EDZ4-anlt	0.0093 *(0.85%)*	0.0226 *(0.83%)*	1.9942 *(0.58%)*
	EDZ4-FEM	0.0092 *(1.22%)*	0.0226 *(1.00%)*	1.9960 *(0.49%)*
	LD2-anlt	0.0092 *(1.88%)*	0.0225 *(1.32%)*	1.9864 *(0.97%)*
	LD2-FEM	0.0092 *(1.75%)*	0.0226 *(1.07%)*	1.9881 *(0.89%)*
	LD4-anlt	0.0094 *(0.00%)*	0.0228 *(0.00%)*	2.0059 *(0.00%)*
	LD4-FEM	0.0094 *(0.14%)*	0.0229 *(0.26%)*	2.0078 *(0.09%)*
10	**Ref. [54]**	**0.0074**	**0.0111**	**0.7530**
	ED2-anlt	0.0065 *(12.42%)*	0.0092 *(17.14%)*	0.6294 *(16.42%)*
	ED2-FEM	0.0065 *(12.43%)*	0.0092 *(17.00%)*	0.6287 *(16.52%)*
	ED4-anlt	0.0073 *(1.17%)*	0.0105 *(4.87%)*	0.7151 *(5.04%)*
	ED4-FEM	0.0073 *(1.21%)*	0.0105 *(4.77%)*	0.7138 *(5.21%)*
	EDZ4-anlt	0.0074 *(0.04%)*	0.0111 *(0.06%)*	0.7527 *(0.04%)*
	EDZ4-FEM	0.0074 *(0.04%)*	0.0111 *(0.03%)*	0.7515 *(0.21%)*
	LD2-anlt	0.0074 *(0.15%)*	0.0111 *(0.14%)*	0.7521 *(0.12%)*
	LD2-FEM	0.0074 *(0.08%)*	0.0111 *(0.10%)*	0.7517 *(0.17%)*
	LD4-anlt	0.0074 *(0.00%)*	0.0111 *(0.00%)*	0.7530 *(0.00%)*
	LD4-FEM	0.0074 *(0.07%)*	0.0111 *(0.23%)*	0.7526 *(0.05%)*
100	**Ref. [54]**	**0.0068**	**0.0068**	**0.4347**
	ED2-anlt	0.0068 *(0.15%)*	0.0068 *(0.34%)*	0.4333 *(0.33%)*
	ED2-FEM	0.0068 *(0.13%)*	0.0068 *(0.32%)*	0.4320 *(0.63%)*
	ED4-anlt	0.0068 *(0.00%)*	0.0068 *(0.10%)*	0.4343 *(0.11%)*
	ED4-FEM	0.0068 *(0.00%)*	0.0068 *(0.09%)*	0.4329 *(0.41%)*
	EDZ4-anlt	0.0068 *(0.00%)*	0.0068 *(0.00%)*	0.4347 *(0.00%)*
	EDZ4-FEM	0.0068 *(0.01%)*	0.0068 *(0.02%)*	0.4334 *(0.31%)*
	LD2-anlt	0.0068 *(0.00%)*	0.0068 *(0.00%)*	0.4347 *(0.00%)*
	LD2-FEM	0.0068 *(0.01%)*	0.0068 *(0.02%)*	0.4334 *(0.30%)*
	LD4-anlt	0.0068 *(0.00%)*	0.0068 *(0.00%)*	0.4347 *(0.00%)*
	LD4-FEM	0.0068 *(0.01%)*	0.0068 *(0.02%)*	0.4334 *(0.30%)*

against the exact solution proposed by Pagano [54] and the Navier closed-form solutions obtained with the corresponding plate model. These latter results are identified by the suffix *-anlt*.

Tables 4 and 5 list the non-dimensional displacement and stress values, respectively, for all considered models, along with the percentage error with respect to the reference solution. Three different length-to-thickness ratios have been considered (S = 4, 10, 100). While simple ESL models are sufficiently accurate for the global response of thin plates, high-order LW models are necessary for thick plates and for an accurate prediction of the local transverse stresses. The results show that the N=8 mesh provides converged FEM results with respect to the corresponding closed-form Navier solution, thus confirming the performances for the isotropic plate. Moreover, the same behavior is found for all considered plate models, which means that the QC4 approximation could be successfully extended to arbitrary kinematics including Zig-Zag and LW models.

It is also interesting to illustrate the through-thickness distribution of the response. Figs. 18, 19 and 20 display the distributions of non-dimensional displacements, in-plane stresses and transverse stresses, respectively, obtained for the moderately thick plate (S = 10) and with the high-order ED4 kinematics. All stresses are directly evaluated from the compatible strains by means of the constitutive relation. The distributions of the displacements (Fig. 18) and the in-plane stresses (Fig. 19) agree well with the reference elasticity solution. However, note that the Zig-Zag shape of the u_1 displacement is not captured by the considered ED4 model. Larger discrepancies are obviously obtained in Fig. 20 for the distributions of the transverse shear stresses because of their interlaminar discontinuity, which is typical of any PVD-based formulation. Thanks to the variable kinematics approach, the proposed FE is nonetheless particularly efficient and accurate in the computation of displacements and stresses for multilayered plates.

5. Conclusion

This paper has introduced a new locking-free four-node quadrilateral finite element (FE) for displacement-based variable kinematics plate models expressed through Carrera's Unified Formulation (CUF). The remedy to the shear locking pathology pertains to the B-bar method and consists in a new QC4 approximation that is constructed for the $z-$ constant term of the transverse shear strain only. The robustness and accuracy of the proposed element has been thoroughly assessed by referring to a number of tests that are recommended whenever new FE applications are proposed: classical eigenvalue counts, convergence behavior for thin and thick plates under various boundary and loading conditions, as well as three case studies involving distorted meshes. The numerical results confirmed the superiority of the proposed FE in comparison to classical isoparametric approaches with full or reduced integrations, i.e., it has a correct rank, is free of transverse shear locking and is less sensitive to distorted element shapes, showing a high convergence rate for both displacements and stresses. The proposed variable kinematics FE, implemented as a user subroutine into Abaqus, provides a robust tool for the analysis of composite laminates, for which different models may be used for adapting the computational cost in case of thin or thick plates or whether a global or local response is required.

Further studies shall concern the optimization of the computational

Table 5
Simply-supported (0°/90°/0°) square plate under bi-sinusoidal pressure load: Non-dimensional stresses for length-to-thickness ratios S = 4, 10, 100.

S	Model	$\bar{\sigma}_{11}\left(\frac{e}{2}\right)$	$-\bar{\sigma}_{22}\left(-\frac{e}{6}\right)$	$\bar{\sigma}_{12}\left(-\frac{e}{2}\right)$	$\bar{\sigma}_{13}(0)$	$\bar{\sigma}_{23}(0)$
4	**Ref. [54]**	**0.8008**	**0.5563**	**0.0505**	**0.2559**	**0.2172**
	ED2-anlt	0.4677 *(41.59%)*	0.4473 *(19.60%)*	0.0339 *(32.78%)*	0.1209 *(52.76%)*	0.1248 *(42.54%)*
	ED2-FEM	0.4648 *(41.96%)*	0.4454 *(19.93%)*	0.0338 *(33.11%)*	0.1204 *(52.95%)*	0.1246 *(42.63%)*
	ED4-anlt	0.7864 *(1.80%)*	0.5070 *(8.86%)*	0.0484 *(4.13%)*	0.2050 *(19.88%)*	0.1830 *(15.75%)*
	ED4-FEM	0.7807 *(2.52%)*	0.5042 *(9.36%)*	0.0481 *(4.73%)*	0.2035 *(20.48%)*	0.1824 *(16.04%)*
	EDZ4-anlt	0.7942 *(0.82%)*	0.5504 *(1.06%)*	0.0501 *(0.84%)*	0.2567 *(0.31%)*	0.1843*(15.15%)*
	EDZ4-FEM	0.7904 *(1.31%)*	0.5448 *(2.07%)*	0.0496 *(1.70%)*	0.2552 *(0.29%)*	0.1832*(15.63%)*
	LD2-anlt	0.7873 *(1.70%)*	0.5448 *(2.07%)*	0.0498 *(1.48%)*	0.2518 *(1.60%)*	0.1752 *(19.32%)*
	LD2-FEM	0.7837 *(2.14%)*	0.5422 *(2.53%)*	0.0495 *(1.90%)*	0.2505 *(2.10%)*	0.1750 *(19.44%)*
	LD4-anlt	0.8009 *(0.00%)*	0.5563 *(0.01%)*	0.0505 *(0.00%)*	0.2559 *(0.01%)*	0.2180 *(0.35%)*
	LD4-FEM	0.7974 *(0.44%)*	0.5538 *(0.45%)*	0.0503 *(0.42%)*	0.2546 *(0.50%)*	0.2176 *(0.15%)*
10	**Ref. [54]**	**0.5906**	**0.2882**	**0.0290**	**0.3573**	**0.1228**
	ED2-anlt	0.5168 *(12.49%)*	0.2438 *(15.39%)*	0.0246 *(15.25%)*	0.1375 *(61.52%)*	0.0751 *(38.81%)*
	ED2-FEM	0.5135 *(13.06%)*	0.2427 *(15.80%)*	0.0244 *(15.72%)*	0.1370 *(61.65%)*	0.0749 *(38.96%)*
	ED4-anlt	0.5835 *(1.20%)*	0.2726 *(5.41%)*	0.0280 *(3.39%)*	0.2617 *(26.75%)*	0.1030 *(16.10%)*
	ED4-FEM	0.5795 *(1.87%)*	0.2711 *(5.93%)*	0.0278 *(3.97%)*	0.2597*(27.33%)*	0.1026*(16.41%)*
	EDZ4-anlt	0.5903 *(0.06%)*	0.2881 *(0.05%)*	0.0290 *(0.05%)*	0.3617 *(1.24%)*	0.1031 *(16.05%)*
	EDZ4-FEM	0.5870 *(0.61%)*	0.2861 *(0.71%)*	0.0288 *(0.66%)*	0.3598 *(0.69%)*	0.1025 *(16.52%)*
	LD2-anlt	0.5899 *(0.12%)*	0.2877 *(0.16%)*	0.0289 *(0.14%)*	0.3557 *(0.46%)*	0.0980 *(20.20%)*
	LD2-FEM	0.5865 *(0.69%)*	0.2865 *(0.59%)*	0.0288 *(0.62%)*	0.3543 *(0.83%)*	0.0978 *(20.32%)*
	LD4-anlt	0.5906 *(0.00%)*	0.2882 *(0.00%)*	0.0290 *(0.00%)*	0.3573 *(0.00%)*	0.1228 *(0.06%)*
	LD4-FEM	0.5872 *(0.57%)*	0.2870 *(0.43%)*	0.0288 *(0.48%)*	0.3560 *(0.38%)*	0.1226 *(0.15%)*
100	**Ref. [54]**	**0.5393**	**0.1808**	**0.0214**	**0.3947**	**0.0828**
	ED2-anlt	0.5384 *(0.15%)*	0.1803 *(0.29%)*	0.0213 *(0.24%)*	0.1424 *(63.93%)*	0.0597 *(27.95%)*
	ED2-FEM	0.5350 *(0.78%)*	0.1791 *(0.92%)*	0.0212 *(0.87%)*	0.1419 *(64.05%)*	0.0594 *(28.22%)*
	ED4-anlt	0.5392 *(0.02%)*	0.1806 *(0.09%)*	0.0214 *(0.06%)*	0.2806 *(28.90%)*	0.0734 *(11.33%)*
	ED4-FEM	0.5358 *(0.65%)*	0.1795 *(0.72%)*	0.0212 *(0.69%)*	0.2784 *(29.46%)*	0.0731 *(11.74%)*
	EDZ4-anlt	0.5393 *(0.00%)*	0.1808 *(0.02%)*	0.0214 *(0.00%)*	0.3998 *(1.29%)*	0.0702 *(15.25%)*
	EDZ4-FEM	0.5358 *(0.63%)*	0.1797 *(0.61%)*	0.0212 *(0.63%)*	0.3978 *(0.78%)*	0.0698 *(15.78%)*
	LD2-anlt	0.5393 *(0.00%)*	0.1808 *(0.02%)*	0.0214 *(0.00%)*	0.3934 *(0.34%)*	0.0666 *(19.58%)*
	LD2-FEM	0.5358 *(0.63%)*	0.1797 *(0.61%)*	0.0212 *(0.63%)*	0.3921 *(0.65%)*	0.0664 *(19.87%)*
	LD4-anlt	0.5393 *(0.00%)*	0.1808 *(0.02%)*	0.0214 *(0.00%)*	0.3947 *(0.00%)*	0.0828 *(0.00%)*
	LD4-FEM	0.5359 *(0.63%)*	0.1797 *(0.63%)*	0.0212 *(0.62%)*	0.3934 *(0.32%)*	0.0825 *(0.35%)*

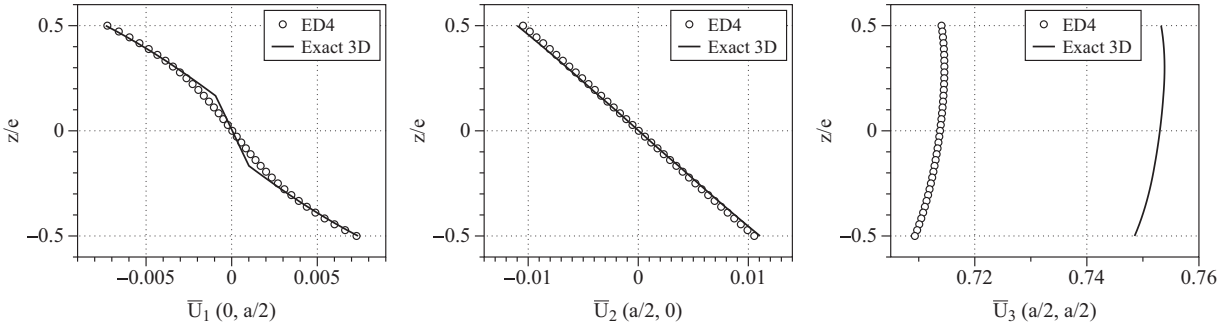

Fig. 18. Through-thickness distribution of $\bar{u}_1$ (left), $\bar{u}_2$ (middle) and $\bar{u}_3$ (right) for the (0°/90°/0°) square plate (S=10).

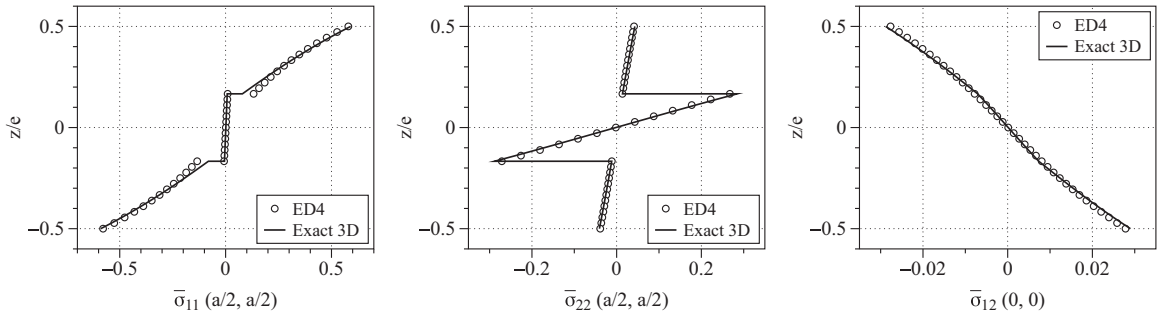

Fig. 19. Through-thickness distribution of $\bar{\sigma}_{11}$ (left), $\bar{\sigma}_{22}$ (middle) and $\bar{\sigma}_{12}$ (right) for the (0°/90°/0°) square plate (S=10).

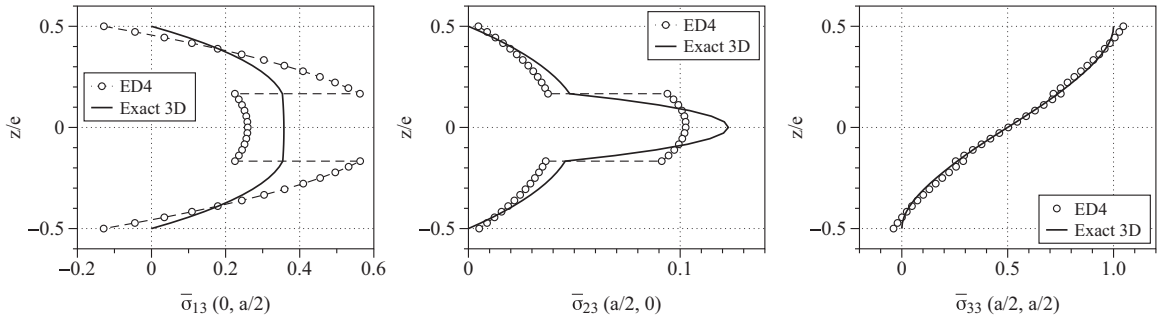

Fig. 20. Through-thickness distribution of $\bar{\sigma}_{13}$ (left), $\bar{\sigma}_{23}$ (middle) and $\bar{\sigma}_{33}$ (right) for the (0°/90°/0°) square plate (S=10).

cost for FE models of composite structures: on the one hand, the FE implementation of a more general variable kinematics modeling approach will be considered [55]; the variable kinematics models shall, on the other hand, be effectively employed within a global-local approach that limits the use of expensive, highly accurate and quasi-3D models to small model portions.

Appendix A. Appendix

A.1. Matrices with thickness functions

The arrays defining the through-thickness behavior of the strain field in Eqs. (14) are

$$\boldsymbol{Fb}_\tau = \begin{bmatrix} 0 & F_\tau & 0 & 0 & 0 & 0 & 0 & 0 & 0 \\ 0 & 0 & 0 & 0 & 0 & F_\tau & 0 & 0 & 0 \\ 0 & 0 & F_\tau & 0 & F_\tau & 0 & 0 & 0 & 0 \end{bmatrix} \tag{A-1a}$$

$$\boldsymbol{Fn}_\tau = [0 \;\; 0 \;\; 0 \;\; 0 \;\; 0 \;\; 0 \;\; F_{\tau,z} \;\; 0 \;\; 0] \tag{A-1b}$$

$$\boldsymbol{Fs}_\tau = \begin{bmatrix} F_{\tau,z} & 0 & 0 & 0 & 0 & 0 & 0 & F_\tau & 0 \\ 0 & 0 & 0 & F_{\tau,z} & 0 & 0 & 0 & 0 & F_\tau \end{bmatrix} \tag{A-1c}$$

The thickness functions describing the $z-$ constant transverse shear strain $\boldsymbol{\gamma}^0$ in Eq. (16) have the following expressions depending on the model:

- ESL model: the following matrices are used for all expansion orders $N \geq 1$:

$$\begin{aligned} \boldsymbol{Fs}^0_{(\tau=0)} &= \begin{bmatrix} 0 & 0 & 0 & 0 & 0 & 0 & 0 & 1 & 0 \\ 0 & 0 & 0 & 0 & 0 & 0 & 0 & 0 & 1 \end{bmatrix} \\ \boldsymbol{Fs}^0_{(\tau=1)} &= \begin{bmatrix} 1 & 0 & 0 & 0 & 0 & 0 & 0 & 0 & 0 \\ 0 & 0 & 0 & 1 & 0 & 0 & 0 & 0 & 0 \end{bmatrix} \end{aligned} \tag{A-2}$$

- LW model: with reference to the notation in Eq. (3), the approximation is defined as $\boldsymbol{Fs}^0_\tau = \boldsymbol{Fs}^0_t + \boldsymbol{Fs}^0_b + \boldsymbol{Fs}^0_r$ (with r = 2, 3, 4), as follows:

$$\begin{aligned} \boldsymbol{Fs}^0_t &= \begin{bmatrix} \frac{1}{e^{(k)}} & 0 & 0 & 0 & 0 & 0 & 0 & \frac{1}{2} & 0 \\ 0 & 0 & 0 & \frac{1}{e^{(k)}} & 0 & 0 & 0 & 0 & \frac{1}{2} \end{bmatrix} \\ \boldsymbol{Fs}^0_b &= \begin{bmatrix} -\frac{1}{e^{(k)}} & 0 & 0 & 0 & 0 & 0 & 0 & \frac{1}{2} & 0 \\ 0 & 0 & 0 & -\frac{1}{e^{(k)}} & 0 & 0 & 0 & 0 & \frac{1}{2} \end{bmatrix} \\ \boldsymbol{Fs}^0_{(r=2)} &= \begin{bmatrix} 0 & 0 & 0 & 0 & 0 & 0 & 0 & -\frac{3}{2} & 0 \\ 0 & 0 & 0 & 0 & 0 & 0 & 0 & 0 & -\frac{3}{2} \end{bmatrix} \\ \boldsymbol{Fs}^0_{(r=3)} &= \begin{bmatrix} -\frac{5}{e^{(k)}} & 0 & 0 & 0 & 0 & 0 & 0 & 0 & 0 \\ 0 & 0 & 0 & -\frac{5}{e^{(k)}} & 0 & 0 & 0 & 0 & 0 \end{bmatrix} \\ \boldsymbol{Fs}^0_{(r=4)} &= \begin{bmatrix} 0 & 0 & 0 & 0 & 0 & 0 & 0 & \frac{7}{8} & 0 \\ 0 & 0 & 0 & 0 & 0 & 0 & 0 & 0 & \frac{7}{8} \end{bmatrix} \end{aligned} \tag{A-3}$$

A.2. QC4 interpolation

The non-zero terms of the 9×3 matrices $\overline{\boldsymbol{B}}_i \quad (i = 1 - 4)$ that define the QC4 interpolation for $\boldsymbol{\gamma}^0$ as in Eq. (31) are

$$
\begin{aligned}
\overline{\boldsymbol{B}}_1(1,1) &= \tfrac{1}{4}(1-\eta)J_{11}^{(1)}; \quad \overline{\boldsymbol{B}}_1(1,2) = \tfrac{1}{4}(1-\eta)J_{12}^{(1)}; \quad \overline{\boldsymbol{B}}_1(8,3) = -\tfrac{1}{4}(1-\eta);\\
\overline{\boldsymbol{B}}_1(4,1) &= \tfrac{1}{4}(1-\xi)J_{21}^{(1)}; \quad \overline{\boldsymbol{B}}_1(4,2) = \tfrac{1}{4}(1-\xi)J_{22}^{(1)}; \quad \overline{\boldsymbol{B}}_1(9,3) = -\tfrac{1}{4}(1-\xi);\\
\overline{\boldsymbol{B}}_2(1,1) &= \tfrac{1}{4}(1-\eta)J_{11}^{(2)}; \quad \overline{\boldsymbol{B}}_2(1,2) = \tfrac{1}{4}(1-\eta)J_{12}^{(2)}; \quad \overline{\boldsymbol{B}}_2(8,3) = \tfrac{1}{4}(1-\eta);\\
\overline{\boldsymbol{B}}_2(4,1) &= \tfrac{1}{4}(1+\xi)J_{21}^{(2)}; \quad \overline{\boldsymbol{B}}_2(4,2) = \tfrac{1}{4}(1+\xi)J_{22}^{(2)}; \quad \overline{\boldsymbol{B}}_2(9,3) = -\tfrac{1}{4}(1+\xi);\\
\overline{\boldsymbol{B}}_3(1,1) &= \tfrac{1}{4}(1+\eta)J_{11}^{(3)}; \quad \overline{\boldsymbol{B}}_3(1,2) = \tfrac{1}{4}(1+\eta)J_{12}^{(3)}; \quad \overline{\boldsymbol{B}}_3(8,3) = \tfrac{1}{4}(1+\eta);\\
\overline{\boldsymbol{B}}_3(4,1) &= \tfrac{1}{4}(1+\xi)J_{21}^{(3)}; \quad \overline{\boldsymbol{B}}_3(4,2) = \tfrac{1}{4}(1+\xi)J_{22}^{(3)}; \quad \overline{\boldsymbol{B}}_3(9,3) = \tfrac{1}{4}(1+\xi);\\
\overline{\boldsymbol{B}}_4(1,1) &= \tfrac{1}{4}(1+\eta)J_{11}^{(4)}; \quad \overline{\boldsymbol{B}}_4(1,2) = \tfrac{1}{4}(1+\eta)J_{12}^{(4)}; \quad \overline{\boldsymbol{B}}_4(8,3) = -\tfrac{1}{4}(1+\eta);\\
\overline{\boldsymbol{B}}_4(4,1) &= \tfrac{1}{4}(1-\xi)J_{21}^{(4)}; \quad \overline{\boldsymbol{B}}_4(4,2) = \tfrac{1}{4}(1-\xi)J_{22}^{(4)}; \quad \overline{\boldsymbol{B}}_4(9,3) = \tfrac{1}{4}(1-\xi);
\end{aligned}
\tag{A-4}
$$

where $J_{\alpha\beta}^{(i)}$ is the Jacobian at node i.

References

[1] A.K. Noor, W.S. Burton, Assessment of shear deformation theories for multilayered composite plates, Appl. Mech. Rev. 42 (1989) 1–13.
[2] J.N. Reddy, D.H. Robbins Jr, Theories and computational models for composite laminates, Appl. Mech. Rev. 47 (1994) 147–169.
[3] A.K. Noor, W.S. Burton, Computational models for sandwich panels and shells, Appl. Mech. Rev. 49 (1996) 155–199.
[4] E. Carrera, Theories and finite elements for multilayered, anisotropic, composite plates and shells, Arch. Comput. Methods Eng. 9 (2002) 87–140.
[5] A.S. Sayyad, Y.M. Ghugal, On the free vibration analysis of laminated composite and sandwich plates: a review of recent literature with some numerical results, Compos. Struct. 129 (2015) 177–201.
[6] J.N. Reddy, Mechanics of Laminated Composite Plates and Shells: theory and Analysis, 2nd Edition, CRC Press, 2004.
[7] J.N. Reddy, A simple higher-order theory for laminated composite plates, J. Appl. Mech. 51 (1984) 745–752.
[8] M. Touratier, An efficient standard plate theory, Int. J. Eng. Sci. 29 (1991) 901–916.
[9] E. Carrera, $C^0_{z\text{-Requirements}}$ - models for the two dimensional analysis of multilayered structures, Compos. Struct. 37 (1997) 373–383.
[10] P. Vidal, O. Polit, A refined sinus plate finite element for laminated and sandwich structures under mechanical and thermomechanical loads, Comput. Methods Appl. Mech. Eng. 253 (2013) 396–412.
[11] A. Tessler, Refined zigzag theory for homogeneous, laminated composite, and sandwich beams derived from Reissner's mixed variational principle, Meccanica 50 (2015) 2621–2648.
[12] E. Carrera, Historical review of zig-zag theories for multilayered plates and shells, Appl. Mech. Rev. 56 (2003) 287–308.
[13] K.H. Lo, R.M. Christensen, E.M. Wu, A high-order theory of plate deformation - Part 1: homogeneous plates - Part 2: laminated plates, J. Appl. Mech. 44 (1977) 663–668 (669-676).
[14] A. Barut, E. Madenci, A. Tessler, C^0-continuous triangular plate element for laminated composite and sandwich plates using the {2,2}-Refined Zigzag Theory, Compos. Struct. 106 (2013) 835–853.
[15] P. Vidal, O. Polit, M. D'Ottavio, E. Valot, Assessment of the refined sinus plate finite element: free edge effect and Meyer-Piening sandwich test, Finite Elem. Anal. Des. 92 (2014) 60–71.
[16] O. Polit, P. Vidal, M. D'Ottavio, Robust C^0 high-order plate finite element for thin to very thick structures: mechanical and thermo-mechanical analysis, Int. J. Numer. Methods Eng. 90 (2012) 429–451.
[17] W. Feng, S.V. Hoa, Partial hybrid finite elements for composite laminates, Finite Elem. Anal. Des. 30 (1998) 365–382.
[18] H. Hu, S. Belouettar, M. Potier-Ferry, E.M. Daya, Multi-scale modelling of sandwich structures using the Arlequin method - Part I: linear modelling, Finite Elem. Anal. Des. 45 (2009) 37–51.
[19] C. Wenzel, P. Vidal, M. D'Ottavio, O. Polit, Coupling of heterogeneous kinematics and finite element approximations applied to composite beam structures, Compos. Struct. 116 (2014) 177–192.
[20] J.N. Reddy, An evaluation of equivalent-single-layer and layerwise theories of composite laminates, Compos. Struct. 25 (1993) 21–35.
[21] F. Biscani, G. Giunta, S. Belouettar, E. Carrera, H. Hu, Variable kinematic plate elements coupled via Arlequin method, Int. J. Numer. Methods Eng. 91 (2012) 1264–1290.
[22] E. Carrera, A. Pagani, M. Petrolo, Use of Lagrange multipliers to combine 1D variable kinematic finite elements, Comput. Struct. 129 (2013) 194–206.
[23] E. Carrera, M. Cinefra, M. Petrolo, E. Zappino, Finite Element Analysis of Structures through Unified Formulation, John Wiley & Sons, Ltd, (2014).
[24] E. Carrera, L. Demasi, Classical and advanced multilayered plate elements based upon PVD and RMVT. Part 1: derivation of finite element matrices. Part 2: numerical implementations, Int. J. Numer. Methods Eng. 55 (2002) 191–231 (253–291).
[25] M. D'Ottavio, F.K. Wittel, J. Reiser, Damage and its evolution in fiber-composite materials: simulation and non-destructive evaluation, in: G. Busse, B. Kröplin, F.K. Wittel (Eds.), Mechanism Based Toolbox: Prototypical Implementation of Tools, ISD Verlag, 2006, pp. 481–518.
[26] M. D'Ottavio, P. Vidal, E. Valot, O. Polit, Assessment of plate theories for free-edge effects, Composites B 48 (2013) 111–121.
[27] C. Wenzel, M. D'Ottavio, O. Polit, P. Vidal, Assessment of free-edge singularities in composite laminates using higher-order plate elements, Mech. Adv. Mater. Struct. 23 (2016) 948–959.
[28] R.H. MacNeal, Perspective on finite elements for shell analysis, Finite Elem. Anal. Des. 30 (1998) 175–186.
[29] T.H.H. Pian, K. Sumihara, State-of-the-art development of hybrid/mixed finite element method, Finite Elem. Anal. Des. 21 (1995) 5–20.
[30] T. Belytschko, W.K. Liu, B. Moran, Nonlinear Finite Elements for Continua and Structures, 2nd Edition, John Wiley & Sons, LTD, (2000).
[31] T.J.R. Hughes, The Finite Element Method, Prentice-Hall, 1987.
[32] T.J.R. Hughes, T. Tezduyar, Finite elements based upon Mindlin plate theory with particular reference to the four node bilinear isoparametric element, J. Appl. Mech. 46 (1981) 587–596.
[33] R.H. MacNeal, Derivation of element stiffness matrices by assumed strain distributions, Nucl. Eng. Des. 70 (1982) 3–12.
[34] K.C. Park, E. Pramono, G.M. Stanley, H.A. Cabiness, The ANS shell elements: earlier developments and recent improvements, in: A. K. Noor, T. Belytschko, J. C. Simo (Eds.), Analytical and Computational Models of Shells, Vol. 3 of CED, ASME, (1989), pp. 217–239.
[35] K.J. Bathe, E.N. Dvorkin, A four-node plate bending element based on Mindlin/Reissner plate theory and a mixed interpolation, Int. J. Numer. Methods Eng. 21 (1985) 367–383.
[36] B.R. Somashekar, G. Prathap, C.R. Babu, A field-consistent, four-noded, laminated, anisotropic plate/shell element, Comput. Struct. 25 (1987) 345–353.
[37] J.-L. Batoz, P. Lardeur, A discrete shear triangular nine d.o.f. element for the analysis of thick to very thin plates, Int. J. Numer. Methods Eng. 28 (1989) 533–560.
[38] K.-U. Bletzinger, M. Bischoff, E. Ramm, A unified approach for shear locking free triangular and rectangular shell finite elements, Comput. Struct. 75 (2000) 321–334.
[39] D.H. Robbins, J.N. Reddy Jr., Modelling of thick composites using a layerwise laminate theory, Int. J. Numer. Methods Eng. 36 (1993) 655–677.
[40] M. D'Ottavio, D. Ballhause, T. Wallmersperger, B. Kröplin, Considerations on higher-order finite elements for multilayered plates based on a unified formulation, Comput. Struct. 84 (2006) 1222–1235.
[41] E. Carrera, M. Cinefra, P. Nali, MITC technique extended to variable kinematic multilayered plate elements, Compos. Struct. 92 (2010) 1888–1895.
[42] G.M. Kulikov, S.V. Plotnikova, A hybrid-mixed four-node quadrilateral plate element based on sampling surfaces method for 3D stress analysis, Int. J. Numer. Methods Eng. 108 (2016) 26–54.
[43] K.Y. Sze, Three-dimensional continuum finite element models for plate/shell analysis, Prog. Struct. Eng. Mater. 4 (2002) 400–407.
[44] N. Büchter, E. Ramm, D. Roehl, Three-dimensional extension of nonlinear shell formulation based on the enhanced assumed strain concept, Int. J. Numer. Methods Eng. 37 (1994) 2551–2568.
[45] H. Naceur, S. Shiri, D. Coutellier, J.-L. Batoz, On the modeling and design of composite multilayered structures using solid-shell finite element model, Finite Elem. Anal. Des. 70–71 (2013) 1–14.
[46] G.M. Kulikov, S.V. Plotnikova, Non-linear geometrically exact assumed stress-strain four-node solid-shell element with high coarse-mesh accuracy, Finite Elem. Anal. Des. 43 (2007) 425–443.
[47] O. Polit, M. Touratier, P. Lory, A new eight-node quadrilateral shear-bending plate finite element, Int. J. Numer. Methods Eng. 37 (1994) 387–411.

[48] R.H. MacNeal, R. Harder, A proposed standard set of problems to test finite element accuracy, Finite Elem. Anal. Des. 1 (1985) 3–20.
[49] H. Murakami, Laminated composite plate theory with improved in-plane response, J. Appl. Mech. 53 (1986) 661–666.
[50] L. Demasi, Partially Zig-Zag advanced higher order shear deformation theories based on the Generalized Unified Formulation, Compos. Struct. 94 (2012) 363–375.
[51] S.P. Timoshenko, S. Woinowsky-Krieger, Theory of Plates and Shells, 2nd Edition, McGraw-Hill, 1959.
[52] A. Razzaque, Program for triangular bending elements with derivative smoothing, Int. J. Numer. Methods Eng. 6 (1973) 333–343.
[53] J.-L. Batoz, G. Dhatt, Modélisation des Structures par Eléments Finis, Vol. 2: Poutres et Plaques, Hermès, 1990.
[54] N.J. Pagano, Exact solutions for rectangular bidirectional composites and sandwich plates, J. Compos. Mater. 4 (1970) 20–34.
[55] M. D'Ottavio, A Sublaminate Generalized Unified Formulation for the analysis of composite structures and its application to sandwich plates bending, Compos. Struct. 142 (2016) 187–199.